Smart Materials in Medicine 4 (2023) 522–537

Contents lists available at ScienceDirect

Smart Materials in Medicine

journal homepage: www.keaipublishing.com/en/journals/smart-materials-in-medicine/

Eggshell-derived amorphous calcium phosphate: Synthesis, characterization and bio-functions as bone graft materials in novel 3D osteoblastic spheroids model

Qianli Ma [a,f], Kristaps Rubenis [b,c], Ólafur Eysteinn Sigurjónsson [d,e], Torben Hildebrand [a], Therese Standal [g,h], Signe Zemjane [b,c], Janis Locs [b,c], Dagnija Loca [b,c], Håvard Jostein Haugen [a,*]

[a] Department of Biomaterials, University of Oslo, Oslo, 0317, Norway
[b] Rudolfs Cimdins Riga Biomaterials Innovations and Development Centre, Institute of General Chemical Engineering, Faculty of Materials Science and Applied Chemistry, Riga Technical University, Riga, Latvia
[c] Baltic Biomaterials Centre of Excellence, Headquarters at Riga Technical University, Riga, Latvia
[d] School of Science and Engineering, Reykjavík University, Reykjavík, Iceland
[e] The Blood Bank, Landspitali-The National University Hospital of Iceland, Reykjavík, Iceland
[f] Department of Immunology, School of Basic Medicine, Fourth Military Medical University, Xi'an, 710032, PR China
[g] Department of Clinical and Molecular Medicine, Norwegian University of Science and Technology, Trondheim, 7491, Norway
[h] Department of Hematology, St.Olavs University Hospital, Trondheim, 7491, Norway

ARTICLE INFO

Keywords:
Eggshell
Bone graft materials
Waste utilization
Amorphous calcium phosphate
Osteoblastic spheroid

ABSTRACT

A multitude of autogenous/allogeneic and semi-synthetic bone graft materials have been developed to reconstruct the defective bone tissue but with high bio-cost and potential environmental pollution. With high calcium content and several trace elements, chicken eggshells are no longer considered as wastes but attractive sources of high-value-added biomaterials. This study used chicken eggshells and synthetic hydroxyapatite (HAp) to synthesize amorphous calcium phosphate (ACP) bone graft materials, namely Control and Eggshell. The physiochemical characteristics, biosafety, and immunocompatibility of synthetic ACP particles were inspected. Their osteogenic activity was further investigated in a novel osteoblastic spheroids model. Eggshell ACP particles exhibited ideal cytocompatibility compared to the control ACP and were more resistant to re-crystallization. In osteoblastic spheroids, Eggshell ACP mediated typical osteogenic mRNA profiles of MC-3T3-E1 cells, accompanied by the increased formation of mineralized nodules and boosted synthesis of ECM proteins represented by OPN and collagen I. This study establishes a promising technique to synthesize stable, safe, and osteoinductive ACP graft particles from eggshell waste. Furthermore, the osteoblastic spheroids constructed in the present study provide a more practical model for biomaterial research, which reflect the three-dimensional interaction between host bone tissue and graft materials more realistically.

1. Introduction

Bone fracture, defect, tooth loss, maxillofacial defect, and deformity are with high clinical incidence. Endosseous graft materials have been widely used to reconstruct the normal functions of defective tissue [1]. According to the species origin of the donor, bone graft materials can be briefly divided into autologous/allogeneic, xenogeneic, and synthetic materials. Albeit autogenous and allogeneic bone grafts contain osteoinductive protein and osteoblastic cells capable of synthesizing new bone and a structural matrix that acts as a scaffold, making it the "gold standard" for bone reconstruction, the limited supply, donor-site morbidity, as well as disease transmission, limit their large-scale commercialization [1,2]. In contrast, semi-synthetic xenogeneic graft materials (e.g., calcined xeno-bone) have been involved in a large number of surgical applications with huge market volume (US$664 million by 2021) [3] due to their ideal biosafety and relatively sufficient supply. However, most commercially available xenograft materials are prepared from mammalian tissue (e.g., porcine and bovine bone/tendon) with heavy bio-cost and highly relevant to the scale of animal husbandry, which also elicits environmental pollution as well as potential ethical

* Corresponding author.
E-mail address: h.j.haugen@odont.uio.no (H.J. Haugen).

https://doi.org/10.1016/j.smaim.2023.04.001
Received 20 February 2023; Received in revised form 30 March 2023; Accepted 3 April 2023
Available online 6 April 2023

issues, especially in less developed areas [4–6]. Therefore, one top priority of bone graft materials development is to obtain safe, modifiable, and environmentally friendly novel synthetic biomaterials capable of replacing autografts/allografts with sufficient supply and ideal osteogenic activity.

Regarding the composition of natural bone tissue (~70% of inorganic compounds, calcium phosphate (CaP) substrate embedded within ~30% of organic compounds, mainly collagens, etc.) [7], several synthetic CaP materials were developed and used as bone substitutes or implant coating materials, with different Ca:P ratios and rates of absorption, such as crystallized hydroxyapatite (HAp), tricalcium phosphate (TCP), and biphasic calcium phosphate (BCP, a combination of HAp and β-TCP), calcium deficient hydroxyapatite (CDHA), and amorphous calcium phosphate (ACP), etc. [8–10]. As a representative of crystalized CaP materials, HAp is a synthetic analog of bone apatite and is considered excellent for improving bone formation [11,12]. However, compared to bone apatite, the excessive crystallinity and stoichiometry of synthetic HAp favor its thermostability and mechanical strength at the expense of solubility [13]. With favorable characteristics, such as structural stability, biocompatibility, and high degradation rate, β-TCP has been introduced to prepare BCP materials for compensating the drawbacks of HAp [14–16].

In addition to the well-studied crystalline CaP materials, ACP has recently attracted significant attention due to its variable physicochemical properties, excellent bioactivity, and superior biodegradation. ACP appears initially as a solid phase formed by supersaturation of calcium-phosphorus solution and specific pH, with a Ca/P ratio of about 1.5 and particle size of 40–100 nm [17,18]. As the precursor of the mineral phase of CaP and the storage "pool" of calcium and phosphorus, ACP regulates the speed of bone formation and enhances the mechanical properties of bone tissue by adjusting Ca/P content in host tissue [19]. In an aqueous solution, metastable ACP could rapidly dissolve and release Ca^{2+} and PO_4^{3-}, followed by the continuous transformation and growth of HAp (re-crystallization) [20]. Growing *in vivo* evidence indicates that ACP could be deposited by intracellular vesicles at the gap zones of collagen matrix fibrils and mediates the growth of bone apatite as a precursor phase in rapidly growing bone tissue [21–26]. *In vitro* studies reported the presence of ACP in the gap zone of collagen fibrils prior to the bone apatite-like structure formation [25,27], as well as the mineralization of type I collagen [28]. Moreover, Popp et al. reported that ACP directly supported the growth and differentiation of osteoblastic lineage cells [29]. ACP micron-fibers sponge was also proved to have an excellent osteoconduction and favored the maturation of human alveolar bone [30]. Compared with HAp, Zr-hybridized ACP particles have shown higher osteogenic activity than HAp, evidenced by increased proliferation, ALP synthesis, and OPN production in osteoblastic MC-3T3-E1 cells [31].

Albeit the synthetic CaP materials can provide an essential inorganic source of Ca/P and mineralized cores for bone formation, the importance of trace elements in natural bone tissue (e.g., Mg, Na, Sr, K, Si, Zn, F, Mn, Fe and B. Etc.) cannot be ignored [32,33], which is known to promote osteogenesis/angiogenesis [33,34] by mediating the nonstoichiometric property and calcium-deficiency of CaP substrates in natural bone tissue [35–37]. Thus, introducing essential trace elements in conventional CaP substrates is expected to be a potential strategy for obtaining biomimetic bone grafts. Furthermore, the abundant calcium (94% $CaCO_3$ and 1% $Ca_3(PO_4)_2$), Mg^{2+} (1% $MgCO_3$), and trace amounts of Mg (3472–4500 ppm), Na (1512 ppm), Sr (320–411 ppm), K (524 ppm), and S (589 ppm) in chicken eggshells, a large-scale (millions of tons every year) product-specific biomineralized food waste, make them an attractive precursor for synthesizing the trace element-doped CaP substrates [38–42]. While many studies on converting eggshells to HAp or β-TCP as bone tissue engineering (TE) scaffolds, eggshell-derived ACP has received little attention, mainly because of its metastability [43,44]. Intriguingly, the trace elements in eggshells, particularly Mg and Sr, are expected to markedly improve the stability of the synthetic ACP through a native One-Pot synthesis [44–46].

The traditional *in vitro* research models for evaluating the bioactivity of biomaterials are mainly based on 2D cell culture but fail to fully reflect the multilayer cellular structure of healthy tissue [47,48]. On the contrary, a 3D culture system could be an ideal solution for mimicking the spatial specificity of *in vivo* tissue during organogenesis and differentiation [48]. Cell spheroids exhibit a 3D multicellular culture system that provides intrinsic tissue morphology and phenotypic properties identical to the *in vivo* milieu [49,50]. As a well-studied model for tumor research, it has been reported that the cells in spheroids showed higher resistance against anti-tumor medicine [51,52]. Therefore, it is necessary to introduce 3D spheroids in this study to comprehensively analyze cell-material interactions and better predict the *in vivo* bioactivity of grafted materials. Various strategies can be used to generate spheroids, such as active generation (rotating flask, low-adherent plates, etc.) [53,54] and passive generation (hydrogel trapping, microfabrication, magnetic levitation, shape-guided aggregation) [52,55,56]. Notably, the size of cell aggregates can significantly affect the behaviors of cells inside the 3D spheroids because of the nutrient supply and hypoxia [57]. Small spheroids (actively generated, <250 μm) have a relatively loose structure with better nutrients/oxygen supply. In contrast, larger spheroids (passively generated, >600 μm) could maintain more delicate structures but may face the threat of hypoxic and over-condensed cellular cores at the center [57]. However, small spheroids are probably not the best choice for studying the cell-material interactions due to their limited internal space to accommodate sufficient particle materials. Some physicochemical stimuli (alginate gel, magnetic beads, etc.) [52,55,56] may be introduced in the passive generation of spheroids, resulting in unexpected interventions. In addition, although some active generation strategies can also generate large cell spheroids (1–2 mm, heterogeneous, such as ClinoReactor-Celvivo), it is difficult for cells to wrap ACP particles actively due to the different specific gravity of ACP particles and cells. Therefore, shape-induced generation may be the most suitable strategy for preparing cell spheroids in this study. This strategy enables the embedding of ACP particles into large-sized homogeneous cell spheroids by taking advantage of different sedimentation rates of ACP and cells.

Considering the metastability of ACP synthesized from a conventional Ca/P double decomposition system, our own-developed dissolution-precipitation method [58] was employed in this study to synthesize ACP particles from HAp and eggshells. Such synthetic ACP particles with improved stability, namely Control and Eggshell ACP, possess similar dimensions and chemical composition but are distinct in nanostructure and re-crystallization resistance. A low-cost shape-guided aggregation technique was applied to establish the 3D osteoblastic spheroids embedded with Control and Eggshell ACP particles. Comprehensive *in vitro* experiments were conducted to systematically examine the biosafety, immunocompatibility, and osteogenic activity of synthetic ACP biomaterials. The results obtained in this study enable a promising strategy for converting large amounts of food waste into high-value-added synthetic bone graft materials with excellent bioactivity. Furthermore, the osteoblastic spheroids constructed in this study provided a more practical model for biomaterial research, more realistically reflecting the 3D spatial interactions between host tissue and bone graft materials.

2. Materials and methods

2.1. Synthesis and sterilization of ACP particles

1) The "control" ACP was synthesized by the previously described dissolution-precipitation method [58]. First, 10 g of HAp powder (#04238; Sigma-Aldrich, USA) was added to 600 mL of deionized water (dH_2O) that was magnetically stirred at 200 rpm. After 10 min, 3 M HCl solution (64.46 mL) was added to the obtained HAp suspension that resulted in the dissolution of HAp. 10 min after the acid was added, the stirring rate of the solution was increased to 600 rpm,

and 2 M NaOH aqueous solution (91.5 mL) was rapidly poured into it. The pH of the synthesis media increased to ~11.0 and led to the formation of a white precipitate. After 5 min, the stirring was discontinued and the precipitate was filtered and washed on a filter paper with dH_2O. Then the precipitate was transferred to plastic containers that subsequently were immersed in liquid nitrogen. Freeze drying was used to remove the excess water from the frozen precipitate. To synthesize the "Eggshell" ACP, eggshells (provided by eggs and egg-product producer "Balticovo" (Lecava, Latvia) were firstly thermally treated at 900 °C for 1 h to decompose the organic matter and transformed $CaCO_3$ to CaO. Then 5.55 g of the obtained CaO was added to 600 mL of dH_2O that was magnetically stirred at 200 rpm. The addition of CaO resulted in the formation of a white suspension. After 10 min, 12.47 mL of 4.76 M H_3PO_4 solution was added to the suspension. The rest of the synthesis steps starting from the HCl solution addition step are the same as described in the "control" ACP synthesis.

2) To avoid unwanted biological and chemical contamination, ACP particles were cleaned and sterilized before the biological experiments. In brief, ACP particles were resuspended in dH_2O (0.1 g/5 ml), centrifuged at 2400 rpm for 2 min, and the supernatant was completely discarded. Afterward, ACP particles were resuspended again in 75% ethanol for 30 min applying an orbital shaker. After spinning down, the particles were rewashed with absolute ethanol, filtered with 0.22 μm sterile syringe filter (CLS431224, Corning, USA), and dried on a heater (45 °C) for 30 min.

2.2. X-ray diffraction (XRD)

XRD patterns of the synthesized ACP particles were collected on a Malvern Panalytical Aeris (Malvern Panalytical, United Kingdom) XRD operated at 40 kV and 15 mA (Cu tube). Diffraction data were collected in the range of 10–70 °2θ, with a step size of 0.04 °2θ. The total measurement time for each sample was 30 min.

2.3. X-ray photoelectron spectroscopy (XPS)

The XPS measurements were performed on a Thetaprobe XP spectrometer (ThermoFisher Scientific, USA) using monochromatic Al Kα radiation ($h\nu = 1486.6$ eV). The analysis area was approximately 400 μm in diameter. The instrument resolution was 2 eV for the "survey" spectra and 0.8 eV for the "detail" spectra, as determined by the full width at half maximum of the Ag 3d5/2 peak obtained on the sputter-cleaned silver. The spectra were acquired in standard acquisition mode. Charge compensation using a combination of low-energy electrons and Ar ions was applied during spectra acquisition. The energy scale was referenced based on the position of the C 1s peak from C–C/C–H bonds in an adventitious carbon set to 284.8 eV binding energy. Quantification was based on the manufacturer's relative sensitivity factors. The treatment of the spectral data was done in Thermo Avantage 5.99 software (ThermoFisher, USA). Peak fitting was performed after subtraction of Shirley backgrounds.

2.4. Scanning electron microscopy (SEM)

To visualize the surface morphology of the synthesized Control and Eggshell ACP particles, Tescan Mira\LMU (Tescan, Czech Republic) SEM was used. The particles were attached to an aluminum specimen stub with double-sided electrically conductive carbon tape. Before examination by SEM, the particles were sputter-coated with Au using an Emitech K550X (Quorum Technologies, United Kingdom) sputter coater. Secondary electrons were used for the image acquisition at an acceleration voltage of 5 kV.

2.5. Transmission electron microscope (TEM)

Control and Eggshell ACP particles were first cleaned in absolute ethanol with ultrasonication for 30 min and then drop-casted on a lacey carbon-supported Cu grid, followed by plasma cleaning. To determine particle size and characterize the morphology of Control and Eggshell ACP particles, JEM-2100F (JEOL, Japan) TEM with a Schottky field emission gun operated at 200 kV was used. TEM images and selected area electron diffraction (SAED) patterns were acquired using a Gatan Orius 200D CCD camera. The particle size (area occupied and mean diameter) of the Control and Eggshell ACP was calculated by Image-Pro plus 6.0 (Image-Pro Plus, Media Cybernetics, Rockville, USA) software.

2.6. Zeta potential measurements

The synthesized Control and Eggshell particles were resuspended in a buffer solution with different pH values (300 μg/ml, citric acid-phosphate buffer, pH 4 to 10). After ultrasonication for 10 min, the suspensions were transferred into detecting cells, and the zeta potential/distribution profiles were detected by Zetasizer Nano ZS (Malvern Panalytical, UK).

2.7. Attenuated total reflection Fourier transform infrared spectroscopy (ATR-FTIR)

The Nicolet iS50 FTIR spectrometer (Thermo Fisher Scientific, USA) with an in-built all-reflective diamond ATR was used to acquire ATR-FTIR spectra of the synthesized Control and Eggshell ACP particles. All spectra were acquired between 400 and 4000 cm^{-1} by co-adding 64 scans (resolution of 4 cm^{-1}). Before acquiring the sample spectrum, the background spectrum was collected and then subtracted from each sample spectrum.

2.8. Inductively Coupled Plasma Mass Spectrometry (ICP-MS)

First, the ACP powders were weighted into a digestion vessel. Then, a concentrated nitric acid (65%, ChemLab, Belgium) was added to the powders to dissolve them, followed by appropriate dilution with dH_2O. The vessels were kept at room temperature for at least 20 min to complete the reaction. Then the vessels were capped and transferred to a Mars 6 (CEM corporation, USA) microwave oven for digestion. The oven temperature was raised to 150 °C within 30 min and held at 150 °C for 30 min, then cooled to room temperature. After cooling, the vessels were opened to release the pressure of evolved gaseous products. The samples were filtered through a filter with a 12–15 μm pore size (Filtres Fioroni, France), quantitatively transferred to volumetric flasks, and diluted to 50 mL volume with dH_2O. An Agilent 7700x ICP-MS (Agilent Technologies, USA) instrument with a Mass Hunter Workstation software for ICP-MS, version B.01.03 (Tokyo, Japan), was used for the analysis of elements.

2.9. Re-crystallization dynamics of ACP biomaterials

ACP particles (Control and Eggshell) were resuspended in α-MEM medium (A1049001, Gibco, USA) with 15% heat-inactivated fetal calf serum (FCS, 20170-106, Gibco, USA) at 37 °C. After 0.5, 1, 2, 4, 8, 16, 14 h, and 7 days, samples were collected and washed (centrifugation at 2400 rpm for 2 min) with dH_2O, 75% ethanol, and absolute ethanol in a sequence. The ACP particles were then dried overnight on a heater (37 °C) and subjected to TEM, SAED, and XRD analysis to inspect their crystallization kinetics.

2.10. Specific surface area (SSA) and true density determination

Quadrasorb™ SI Surface Area and Pore Size Analyzer (Quantachrome Instruments, USA) was used to generate N2 adsorption-desorption isotherms of the synthesized ACP particles at −196 °C. Before the analysis,

the synthesized ACP particles were degassed in the AUTOSORB Degasser (Quantachrome Instruments, USA) for 24 h under vacuum at room temperature. The Brunauer–Emmett–Teller model was used to determine the SSA of the synthesized particles based on their adsorption isotherms in the P/P0 range from 0.05 to 0.3 [59].

Micro UltraPyc™ 1200e helium pycnometer (Quantachrome Instruments, USA) was used to determine the true density of the synthesized ACP particles. The pycnometer was first calibrated with stainless-steel calibration spheres of known volume. Then, the volume of the powdered sample was determined by pressurizing the particle-containing sample cell to a target pressure of 10 psig (pounds per square inch gauge). The measurement was repeated until the percent deviation of five consecutive measurements was $\leq 0.1\%$. The true density value of the sample was calculated by dividing its weight by the measured volume of the sample.

2.11. Endotoxin determination of ACP biomaterials

1) Extract preparation: ACP particles (Control and Eggshell) were treated with sterile endotoxin-free water (TMS-011, Sigma-Aldrich, USA) and PBS (TMS-012, Sigma-Aldrich, USA) solution, respectively, at the concentration of 0.1 g/ml. To obtain the extracts, prepared samples were incubated at 37 °C for 48 h, applying periodical shaking (250 rpm on a microshaker). 2) Pierce™ Limulus Amebocyte Lysate (LAL) Chromogenic Endotoxin Quantitation Kit (88282, ThermoFisher, USA) were used to detect endotoxin level in sample extracts according to the manufacturer's instructions. In brief, sample extracts and each standard (0.1–1.0 EU/ml) were added into the designed 96-well plate with the setting of triplicates/sample. LAL assay was used to treat the samples and standards, and then the absorbance at 405 nm was measured on a microplate reader (iMark, Bio-Rad, USA). The endotoxin level in samples was calculated according to the standard curve.

2.12. Hemolytic toxicity of ACP biomaterials

The study adhered to the tenets of the Declaration of Helsinki. Anti-coagulated fresh human peripheral blood was obtained and processed with ethical and institutional approvals and informed consent. For healthy donors, freshly drawn blood or buffy coats were obtained from St. Olavs Hospital, Trondheim, Norway. The Regional Ethics Committee in Central Norway approved the use of blood/buffy coat from healthy donors, REK# 2009/2245. Ficoll density gradient centrifugation was conducted to obtain Red blood cells(RBCs). In brief, blood was mixed with PBS (1:1 v/v) and placed on the layer of Ficoll® 1077 (GE17-1440-02, Merck, Germany). Obtained samples were centrifuged (1800 rpm at 20 °C for 20 min), and the bottom red pellet (RBCs and granulocytes) was collected. The human lineage cell depletion kit (130-092-211, Miltenyi Biotec, Germany) was used to remove granulocytes. The pure RBCs were gently washed with centrifugation at 450 rpm and resuspended using two different assays: 1) Direct contact assay: ACP particles were mixed with RBCs/cold PBS resuspension (0.1 g/ml, 4 times the original blood volume). 2) Extract assay: RBCs were resuspended in ACP-PBS extracts (prepared as described in section 2.11, 4 times of the original blood volume). Obtained samples were incubated at 37 °C for 0.5, 1, and 2 h with corresponding autohomelysis control (RBCs in blank PBS) and positive hemolysis control (RBCs in blank PBS with 1% TritonX-100 (X100, Sigma-Aldrich, USA)). After incubation, the hemolysis test was immediately performed in a 96-well plate with Hemoglobin Colorimetric Detection Kit (EIAHGBC, Invitrogen, USA) according to the manufacturer's instruction. The absorbance at 570 nm was measured on a microplate reader. Hemoglobin concentration and hemolysis were calculated according to the standard curve and the following equation:

$$\text{Hemolysis}\ (\%) = \frac{Value.Test - Value.Auto}{Value.Positive - Value.Auto} \times 100\%$$

Where *Value.Test* indicates the absorbance value of tested samples; The *Value.Auto* indicates the absorbance value of autohomelysis control; *Value.Positive* indicates the absorbance value of positive hemolysis control.

2.13. Biological functions of ACP biomaterials on monocytic THP-1 cells

Human monocytic cell line THP-1(ATCC, USA) was cultured according to manufacturers' instructions. In brief, THP-1 cells were cultured in phenol red-free RPMI1640 (11835030, Gibco, USA) medium with 10% heat-inactivated fetal calf serum, 10 mM HEPES, 1 mM sodium pyruvate, 4500 mg/L glucose, 50 μM 2-mercaptoethanol (M6250, Merck, Germany) and Penicillin (P, 100units/ml)/Streptomycin (S, 100 μg/ml) at 37 °C with humidified 5% CO_2. Cells were passaged when they reached the density of 1×10^6 cells/ml.

2.13.1. Cytotoxicity of ACP biomaterials

The experimental design was established according to previous studies, ISO standards, and guidance of the LDH testing kit (11644793001, Roche, USA) [60,61]. ACP particles were mixed with RPMI1640 complete medium (0.1 g/ml) and incubated at 37 °C for 48 h with periodic shaking (250 rpm on microshaker) to obtain the conditioned media (CM). For direct contact assay, cell density was adjusted to 3×10^5 cells/ml with fresh medium and mixed with ACP particles (1 ml/0.1 g); for indirect contact assay, cells were resuspended in CM at the same density. Prepared samples were incubated at 37 °C for 48 h with corresponding background control (Blank medium), cell control (THP-1 suspension), and corresponding positive controls (THP-1 cell suspension with 1% TritonX-100 added 0.5 h before sample collection). The procedure was followed with sample centrifugation at 1000 rpm and supernatant collection. The lactic dehydrogenase (LDH) activity was detected with LDH Cytotoxicity Detection Kit as mentioned above. Results were calculated according to the following equation:

$$\text{Cytotoxicity}_{(\text{Test})} = \frac{Value.Test - Value.Cell}{Value.Positive - Value.Cell} \times 100\%$$

Where *Value.Test* indicates the absorbance value of tested samples; *Value.Cell* indicates the absorbance value of cell control; *Value.Positive* indicates the absorbance value of positive toxic control.

2.13.2. Immunocompatibility of ACP biomaterials

Cell culture, ACP stimulation, and sample collection were the same as described above (section 2.13.1) for the direct and indirect assays. The level of pro-inflammatory cytokines (TNF-α, IL-1β, and IL-6) and anti-inflammatory cytokines (IL-4 and IL-10) were detected by ELISA according to the manufacturer's instruction (DY210, DY201, DY204, DY206, DY217B, R&D systems, USA).

2.13.3. Cell proliferation viability

The effects of ACP samples on THP-1 cell proliferation were evaluated by PrestoBlue (A13261, Invitrogen, USA) with direct and indirect assays. The preparation of conditioned media was the same as described in section 2.13.1. For direct contact assay, cell density was adjusted to 3×10^5 cells/ml with fresh medium and ACP particles (1 ml/0.1 g); for indirect contact assay, cells were resuspended in CM at the same density. Obtained samples were incubated at 37 °C for 48 h with corresponding background control (Blank medium), cell control (THP-1 cells in fresh medium), and positive control (THP-1 cells with 1% TritonX-100 added 0.5 h before Prestoblue added). After incubation, 1/10th of Prestoblue solution was added to the cell suspension and incubated for 30 min. Obtained supernatants were transferred to a 96-well plate (100 μl/well), and fluorescent intensity at 540/590 nm (excitation/emission) was determined.

2.14. Osteogenic activity of ACP biomaterials

2.14.1. Culture and establishment of MC-3T3-E1 3D osteoblastic spheroid

MC-3T3-E1 osteoblastic cells (ATCC, USA) were cultured in α-MEM medium with 15% FCS and P/S at 37 °C with humidified 5% CO_2. Cells were passaged at 80% confluency.

1) For 3D spheroids establishment: cells were resuspended and their density of 1×10^6 cells/ml was adjusted. To build the Control cell spheroids, 200 μl cell resuspension per well was seeded into a U-bottom non-adherent 96 well plate (BIOFLOAT ™ 96 well plate, faCellitate, Germany) and cultured for 24 h to obtain osteoblastic spheroids. To build ACP-embedded spheroids, 200 μl cell resuspension per well was seeded in the same BIOFLOAT 96 well plate and cultured for 0.5 h to allow the preliminary sedimentation of the single cell layer, followed by adding ACP particles (100 μg/well) and culturing step for additional 23.5 h to form ACP-embedded osteoblastic spheroids. Then, three groups of spheroids were placed into a new 24-well plate (12 spheroids/well) and cultured in different culture media: a) growth medium (GM), fresh blank culture medium; b) VC medium (VC), GM with 50 μg/ml ascorbic acid (A5960, Sigma-Aldrich, USA); c) osteogenic medium (OM), GM with 50 μg/ml ascorbic acid, 10 mM β-Glycerophosphate (G9422, Sigma-Aldrich, USA) and 100 nM dexamethasone (D4902, Sigma-Aldrich, USA).
2) for the 2D culture system: cells were seeded into the 6-well plate at the density of 2×10^4 cells/ml (4 ml/well) and cultured to 80% confluency. ACP particles were added to the cell layer to form 3 groups: Control Cells (no ACP particles), Control ACP, and Eggshell ACP (in the presence of 4 mg ACP/well). Samples were cultured in GM, VC, and OM as described above.

2.14.2. Real-time quantitative PCR

The ACP treatment and medium grouping were the same as described in 2.14.1. In brief, 2D cells and 3D spheroids were cultured for 1, 3, 7, and 14 days. mRNA from samples was isolated with RNeasy Mini Kit (74104, Qiagen, Germany) and reverse-transcribed to cDNA using High-Capacity RNA-to-cDNA™ Kit (4388950, Applied Biosystems, Thermofisher Scientific, USA) according to the manufactures' instructions. qPCR (CFX96™ PCR System, Bio-rad, USA) was performed with TaqMan Gene Expression Assay, mouse TaqMan probes were all purchased from ThermoFisher Scientific: *ALP* (Mm00475834_m1), *RUNX2* (Mm00501584_m1), *COL1A1* (Mm00801666_g1), *OPN* (Mm00436767_m1), *OCN* (Mm03413826_mH), *GAPDH* (Mm99999915_g1, as housekeeping reference).

2.14.3. Extracellular matrix (ECM) mineralization

The ACP treatment and medium grouping were the same as described in 2.14.1. In brief, cells and spheroids were cultured for 14 days and then fixed with 60% isopropanol (563935, Sigma-Aldrich, USA) for 1 min. After rehydration in dH_20 for 3 min, the samples were stained with 40 mM alizarin red (ARS, PH 4.1, TMS-008, Sigma-Aldrich, Germany) aqueous solution for 3 min. After washing with dH_2O twice, images were taken by a microscope. To quantify the mineralized nodules formation (only 2D culture system), the red stain was dissolved in 10% cetylpyridinium chloride (6004-24-6, Sigma-Aldrich, USA) in 10 mM Na_3PO_4 (342483, Sigma-Aldrich, USA) and the absorbance was measured at 620 nm on a microplate reader.

2.14.4. Extracellular collagen secretion

The ACP treatment and medium grouping were the same as described in 2.14.1. In brief, cells and spheroids were cultured for 14 days and then fixed with 4% paraformaldehyde (PFA, P6148, Sigma-Aldrich, USA) for 20 min. After washing in PBS twice, samples were stained in a 0.1 wt% Sirius Red (365548, Sigma-Aldrich, USA) in the saturated picric acid solution (P6744, Sigma-Aldrich, USA) for 18 h. The samples were then washed with 0.1 M acetic acid (A6283, Sigma-Aldrich, USA), and microscope images were taken. For quantitative analysis (only 2D culture system), stains were eluted in 500 μl elution solution (0.2 M NaOH/methanol 1:1, S5811 and 34860, Sigma-Aldrich, USA), and the absorbance was then measured at 540 nm on the microplate reader.

2.14.5. Immunofluorescent staining and confocal microscope observation

The ACP treatment and medium grouping were the same as described in 2.14.1. In brief, cells and spheroids were cultured for 7 days and then fixed with 4 wt % PFA for 20 min. After washing in PBS thrice, samples were treated with 1% (v/v) TritionX-100 (X100, Sigma-Aldrich, USA) for 20 min, followed by blocking in 1 wt % BSA/PBS solution for 1 h. Then, the samples were incubated in goat-anti-mouse OPN primary antibody (Ab) (AF808, R&D systems, USA) and rabbit-anti-mouse collagen I Ab (ab21286, Abcam, USA) at 4 °C overnight. After incubation, samples were washed in PBS for 5min on a shaker thrice and subjected to the incubation of Alexa Fluor™ 488-labelled Chicken anti-Goat secondary Ab (A21467, Invitrogen, USA) and Alexa Fluor™ 568-labelled Donkey anti-Rabbit secondary Ab (A10042, Invitrogen, USA) for 1 h at room temperature. The cell nuclei were counter-stained with DRAQ5 (62251, Thermo Scientific, USA). After washing with PBS, samples were mounted and observed by laser scanning confocal microscope (LSCM, SP8, Leica, Germany).

2.15. Statistical analysis

Unless otherwise noted, experiments were repeated three times, with three to four replicates in each group. All data were analyzed using SPSS 28.0 (IBM, USA) and are expressed as the mean ± standard deviation for continuous variables. Significant differences between groups were identified using one-way analysis of variance (ANOVA) followed by a Student-Newman-Keuls post hoc test for parametric data or a Kruskal-Wallis test followed by a Dunn's multiple comparison test for non-parametric data. Differences were considered statistically significant when $p < 0.01$. The data were plotted by Origin(Pro) 2022 (for the materials part, OriginLab Corporation, USA) and Prism 9.4.1 (for the biological part, GraphPad Software, USA).

3. Results and discussion

3.1. Characterization of ACP biomaterials

3.1.1. FTIR, XRD, and elemental analysis

Similar, broad, superimposed absorption bands were observed in the FTIR spectra of the Control and Eggshell ACP materials (Fig. 1A). The spectra contained broad, relatively weak absorption bands in the range of 2400–3700 cm^{-1} and narrower bands at about 1650, 1480, 1420, 1000, 950, 870, and 550 cm^{-1}. Some background noise could be observed in the range of 1900–2700 cm^{-1}. Absorption bands at around 550, 950, 1000 cm^{-1} have been assigned to ν_4 PO_4^{3-}, ν_1 PO_4^{3-}, and ν_3 PO_4^{3-} group vibrations, respectively [44]. The bands in the range of 2400–3700 cm^{-1} and around 1640 cm^{-1} have been associated with O–H stretching and bending vibrational modes of water molecules, respectively [62]. The bands in the range of 1420–1480 cm^{-1} have been attributed to ν_3 CO_3^{2-} vibration, while the band at 870 cm^{-1} to ν_2 CO_3^{2-} and HPO_4^{2-} vibrations [63,64]. Although CO_3^{2-} containing chemicals were not used to synthesize ACP, carbonate ions were detected in their structure. Carbonate ions could possibly be incorporated into their structure from the synthesis medium since water quickly absorbs CO_2 from the air. Another source of carbonate ions could be the hydroxyapatite and CaO used to synthesize ACP. Hydroxyapatite and CaO readily adsorb CO_2 from the air. XRD patterns of the Control and Eggshell ACP were identical (Fig. 1B). Only two diffused humps that are characteristic of ACP were observed in their diffraction patterns. Such results proved the chemical composition and amorphous crystalline form of synthetic ACP particles.

XPS spectra analyzed the elemental composition profile. The peaks of calcium, phosphorus, and oxygen can be observed in Fig. 1C and D.

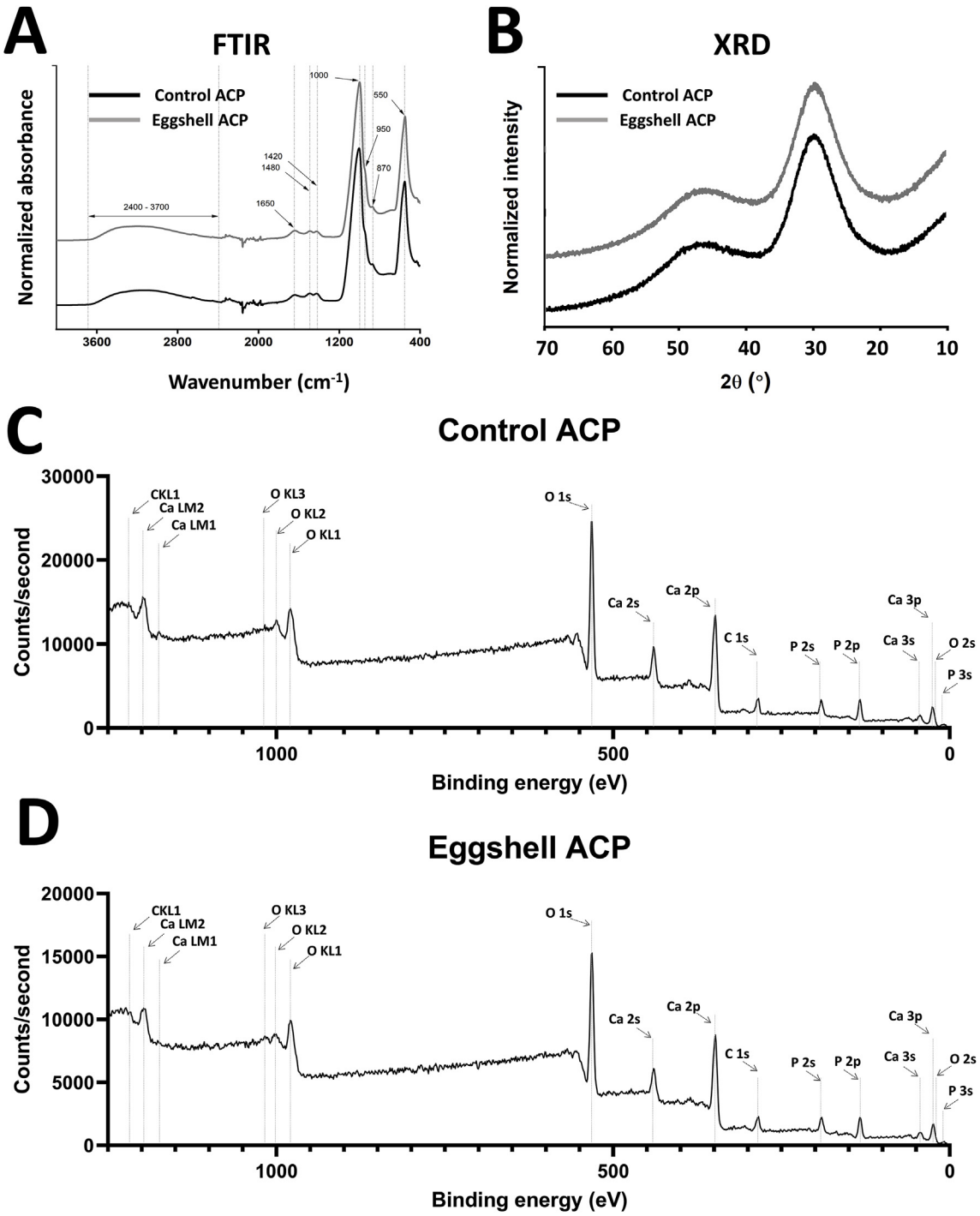

Fig. 1. Chemical-Physical characterization of ACP biomaterials. (A) FTIR spectra of Control and Eggshell ACP materials; (B) XRD pattern of Control and Eggshell ACP materials; (C, D) XPS spectrum of Control and Eggshell ACP materials.

However, no other trace elements were detected by XPS. Regarding the relatively high contents of Mg and Sr in natural eggshells [39–42], the undetected elements may be due to the limited sensitivity of XPS or that they were hard to form precipitation during ACP preparation. Here, high-sensitive ICP-MS was employed to measure the presence of trace elements in both Control and Eggshell ACP. The results in Table .1 demonstrated that more Mg and Sr were detected in Eggshell ACP compared with Control ACP (Mg: 2.20 ± 0.22 g/kg vs. 1.47 ± 0.15 g/kg; Sr: 236 ± 24 mg/kg vs. 121 ± 12 mg/kg). Mg and Sr are crucial for bone regeneration and may facilitate the osteoinductivity of ACP biomaterials, especially Eggshell ACP [65,66]. Control ACP particles had a higher Fe level than Eggshell (114 ± 11 mg/kg vs. <3.33 mg/kg). High concentration of ferric ions not only diminish the proliferation of osteoblasts [67] but also abolish their capacity for osteogenic differentiation and mineralization [68]. The overactivation of osteoclasts induced by ferric ions also contributed to bone resorption [69]. Other elements, such as As, Na, and Cu, were also detected in Control and Eggshell ACP. However, their low absolute concentration or lack of osteogenic activity might not interfere with the bioactivity of ACP materials.

Table 1
Trace elements of Control and Eggshell ACP materials by ICP-MS.

	Control ACP	Eggshell ACP
Mg	1.47 ± 0.15 g/kg	2.20 ± 0.22 g/kg *
Sr	121 ± 12 mg/kg	236 ± 24 mg/kg *
Fe	114 ± 11 mg/kg *	<3.33 mg/kg
As	0.021 ± 0.002 mg/kg	1.29 ± 0.13 mg/kg *
Na	3.13 ± 0.31 g/kg *	1.13 ± 0.11 g/kg
K	<66.7 mg/kg	<66.7 mg/kg
Zn	<6.67 mg/kg	<6.67 mg/kg
Hg	<0.033 mg/kg	<0.033 mg/kg
Cd	0.034 ± 0.003 mg/kg	<0.017 mg/kg
Si	<2 mg/kg	<2 mg/kg
Pb	0.183 ± 0.018 mg/kg	<0.033 mg/kg
Cu	<1.67 mg/kg	2.19 ± mg/kg

*$p < 0.05$.

3.1.2. SEM observation, TEM ultrastructure, and zeta potential of ACP particles

As shown in Fig. 2A and B, and C, the synthesized Control ACP consisted of irregularly shaped micron-sized (63.54 ± 61.66 μm in diameter) agglomerates of nanoparticles, while the Eggshell ACP consisted of smaller nanoparticle agglomerates with narrower size distribution (13.23 ± 9.66 μm in diameter). Primary particle size in the agglomerates of the Control ACP was larger (35.26 ± 8.75 nm) compared with that of the Eggshell ACP (24.51 ± 4.93 nm). SAED images of both Control and Eggshell ACP showed a broad halo ring pattern typical for amorphous materials.

Considering that the ACP basic units may agglomerate and form large particles spontaneously, the zeta potentials of both Control and Eggshell ACP particles were determined. In the pH range from 4 to 10, the Zeta potentials of both Control and Eggshell ACP particles were less than 25 mV (absolute value) and there was no difference between the two groups (Fig. 2E). Such evidence indicated that Control and Eggshell ACP particles have a similar tendency of dispersion dynamics. Moreover, the agglomeration was also apparent in as-synthesized Control ACP particles macroscopically. Control ACP particles were hardly disaggregated by intense ultrasonication, which indicated that more considerable Control ACP particles were probably formed during the synthesis procedure other than in storage. The trace elements in Eggshells may contribute to the improved dispersion of particles.

3.1.3. Re-crystallization dynamics, SSA, and true density of ACP biomaterials

Compared with the high crystallization and stoichiometry of HAp, which leads to a relatively slow dissolution [70], the amorphous structure, hydrated layer, and defects of ACP greatly enhance its solubility. In particular, the lack of periodic long-range order of ACP allows the formation of structural defects, thereby improving its bioactivity by increasing the rates of both solubility and bio-resorption [18]. However, under certain conditions, such as moisture, different organic/inorganic environment, temperatures, etc., the metastable ACP might easily re-crystallize to HAp. Our previous work found that ACP has recrystallized during the cold sintering process at high temperatures (150 °C). Moreover, moisture made this procedure much more accessible with a greatly reduced temperature threshold (150 °C–100 °C) [71]. As bone graft materials, ACP particles will not experience high temperatures but remain embedded in the moist host tissue for a long time. Therefore, the re-crystallization of ACP biomaterials in a liquid environment at body temperature was investigated and depicted in Fig. 3. TEM (Fig. 3A) exhibited that both Control and Eggshell ACP particles kept amorphous morphology within 8 h in an α-MEM complete medium at 37 °C. After incubation for 16 h, the basic nano-unit of Control ACP particles had changed to a "hair-like" ultrastructure. With the increased incubation time, such a "hair-like" structure became more compact. On the contrary, Eggshell ACP started the re-crystallization after 16 h. In addition, the nano-crystals of Eggshell ACP showed a different "short needle-like" ultrastructure compared with Control ACP. XRD spectra gave us more details (Fig. 3B). Eggshell ACP started the re-crystallization from 8 h (with feeble signals), whereas Control ACP started the process from 4 h. Here we can conclude that the primary crystallization process of Eggshell ACP occurs between 8 and 16 h, whereas between 4 and 8 h for Control ACP. SAED quantification (Fig. 1S) also showed a typical "crystalline shoulder," as indicated by red arrows. However, due to the different thicknesses of ACP particles on the TEM copper mesh, images were taken under slightly different defocus values and need further optimization. The different resistant capacities of re-crystallization of Control and Eggshell ACP may be due to the different trace elemental composition in ACP particles (Table .1). Among them, Mg has been documented to be an effective inhibitor for the phase transformation of ACP [45,46]. Sr was also reported to stabilize amorphous minerals [72]. Moreover, it was proved that Mg and Sr could significantly delay the ACP crystallization together, compared with independent Mg or Sr [73]. The coexistence of Mg and Sr led to additional energy barriers for the ACP phase transformation and then provided an improved stabilization on ACP, which might facilitate the host bone formation [73]. As depicted in Table .2, Control and Eggshell ACP shared similar true density, but the SSA of Eggshell ACP was higher than that of Control ACP. Higher SSA provides more contact interface between materials and bio-components (body fluid, cells, culture medium, etc.), which may enhance the interactions between host tissue and implanted materials [74].

3.2. Biosafety of ACP biomaterials

3.2.1. Endotoxin contamination and hemolytic toxicity of ACP biomaterials

A classic LAL assay was performed based on the endotoxin-free PBS and water to measure the endotoxin contamination in synthesized ACP particles. As it is shown in Fig. 4 A, the red dot line indicates the lower detection limit of the LAL Quantitation Kit (0.05 EU/ml). None of the ACP extracts (PBS or water extracts) showed endotoxin contamination over the detection limit. Notably, three water extract groups showed relatively higher endotoxin levels than PBS extract groups, which may be attributed to the different reaction sensitivity of the LAL assay to water and PBS. Therefore, it can be concluded here that simple ethanol washing could remove endotoxin contamination of ACP Particles, which could be used in further biological experiments.

Direct and indirect assays were conducted to measure the hemolytic toxicity of ACP biomaterials. Fig. 4B and **C** showed that ACP extracts (both Control and Eggshell ACP) did not elicit any hemolysis according to the auto-hemolysis control (PBS) within 2 h of incubation. However, ACP particles (both Control and Eggshell ACP) resulted in slight hemolysis after contact with RBCs shortly (0.5 h). Hemolytic activity increased with time but reached a plateau after 1 h (maximum hemolysis < 7% at 2 h). No differences between Control ACP and Eggshell ACP could be observed at any time point. According to the morphology of ACP particles (Fig. 1A), the possible reason for such hemolysis may be that the shape edge of ACP particles injures the vulnerable RBCs. Another speculation might be that the rapidly increased concentration of Ca^{2+} and PO_4^{3+} dissolved from ACP particles may lead to the damage of RBCs. However, it could not explain why ACP extracts did not elicit hemolysis.

3.2.2. Cytocompatibility and immunocompatibility of ACP particles on THP-1 cells

The cytotoxicity of ACP particles was measured by LDH assay, and the relative cell damage was calculated and plotted according to their corresponding positive cytotoxic reference (TritonX-100). Data in Fig. 5 demonstrated that none of the ACP groups (Control or Eggshell, Extracts or ACP particles) exhibited positive cytotoxicity compared with Blank medium or internal control (Control THP-1 cells) (Fig. 5B). Such non-toxic properties of synthesized ACP biomaterials was in accordance with previous research [75]. In addition, the typical pro-/anti-inflammatory cytokines were tested in THP-1 supernatants. According to the cell control, blank medium, and detection limitation of ELISA kits, the

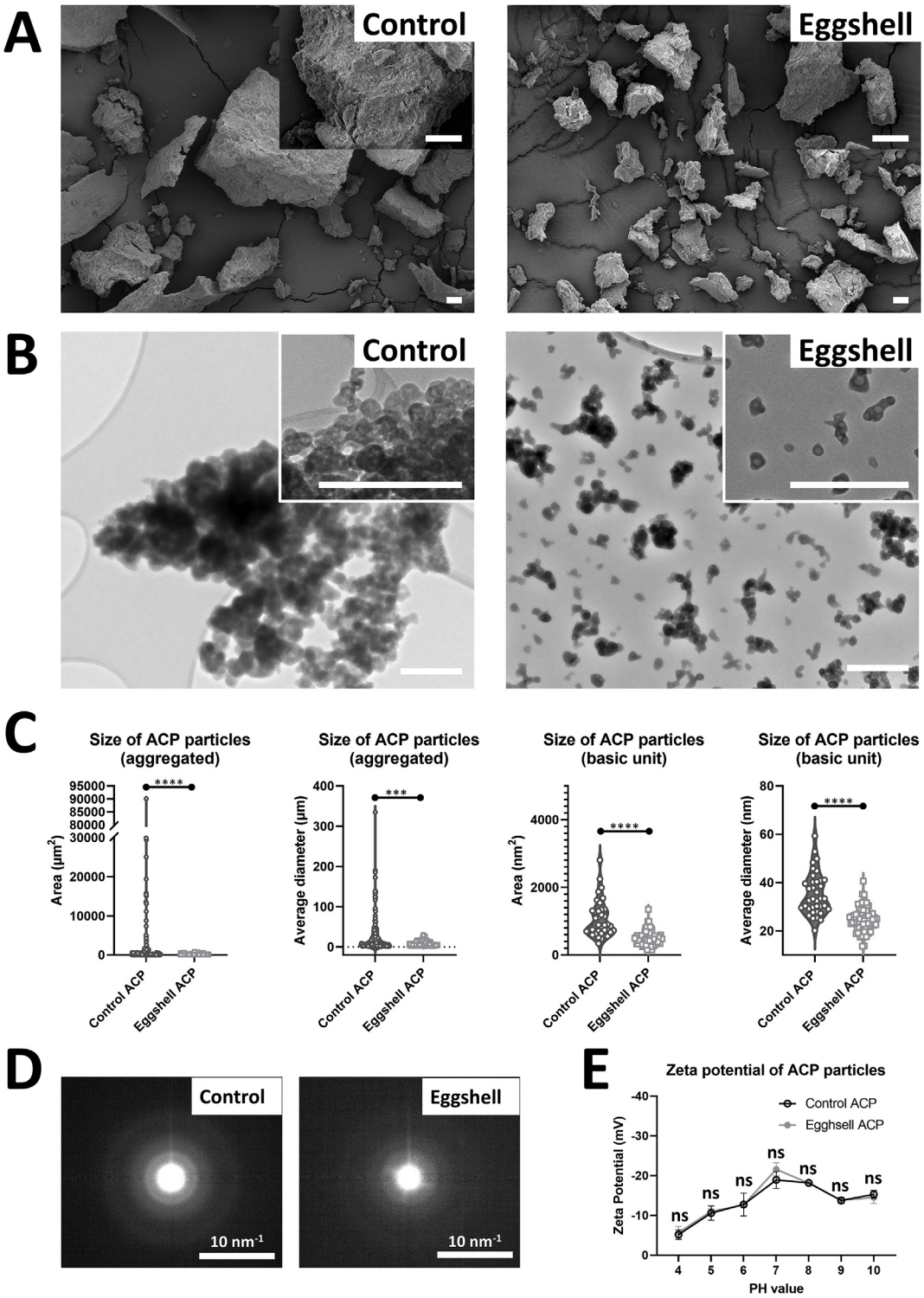

Fig. 2. Ultrastructure analysis and zeta potential of ACP microparticles. (A) SEM images of ACP particles, Scale bar = 10 μm; (B) TEM images of ACP particles, Scale bar = 200 nm; (C) Size of ACP aggregated particles and basic nano-units; (D) SAED images of ACP materials; (D) Zeta potential of ACP particles in different PH value. *, $p < 0.05$; **, $p < 0.01$; ***, $p < 0.001$; ****, $p < 0.0001$; ns, no significance.

results indicated that ACP (particles or extracts) did not elicit any visible inflammatory response of THP-1 monocytic cells and should be tolerant to the host immune system. Furthermore, the host inflammatory responses against CaP materials were widely investigated [76], and HAp and TCP were reported to elicit host inflammation [77,78]. On the contrary, few studies on ACP materials' immunocompatibility were published, even with some controversial conclusions. For example, Feng G et al. reported that ACP nanoparticles (NPs, diameter < 150 nm) could alleviate poly-L-lactic acid implantation-induced host tissue inflammation *in vivo* [79]. Another *in vitro* research reported that ACP NPs facilitated M1 polarization of macrophages and thus formed an inflammatory microenvironment to attenuate host osteogenesis [19]. Nevertheless, the

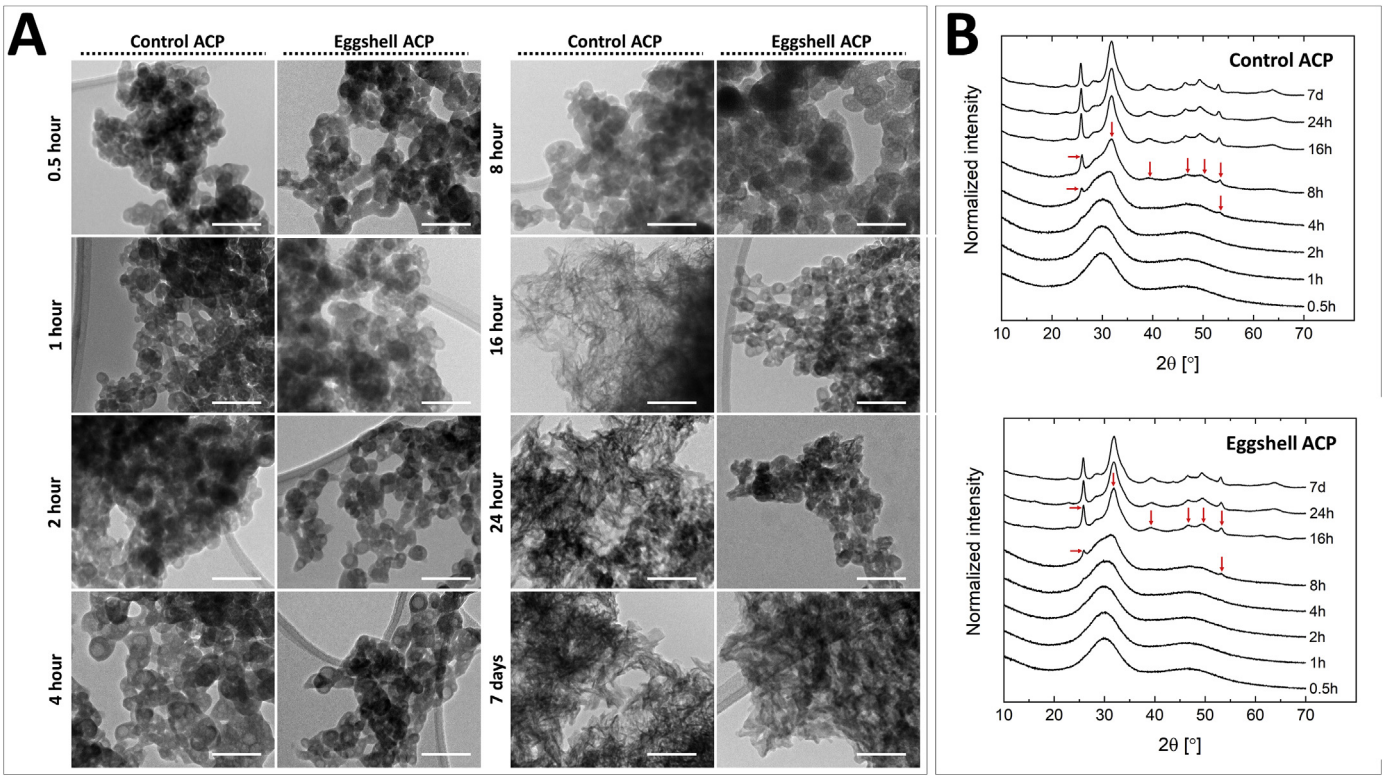

Fig. 3. Re-crystallization dynamics of ACP biomaterials. (A) TEM inspection of ACP crystallization in aqueous solution at 37 °C from 0.5 h to 7 days; (B) XRD pattern of ACP crystallization in aqueous solution at 37 °C from 0.5 h to 7 days. Scale bar = 100 nm; Red arrows, characteristic signals of HAp crystalline.

Table 2
Specific surface area and true density of Control and Eggshell ACP materials.

	Control ACP	Eggshell ACP
Specific surface area	123.1 m^2/g	159.6 m^2/g
True density	2.50 g/cm^3	2.49 g/cm^3

difference in ACP particle size (nanoscale vs. micron-scale) and elemental composition (Sr [80]) could contribute to the divergence between different research.

Since the cytokine secretion may be affected by different cell densities, the PrestoBlue assay was employed to measure the viability of THP-1 cells. As shown in Fig. 6F, ACP extracts and ACP particles (both Control and Eggshell ACP) led to higher THP-1 proliferation viability

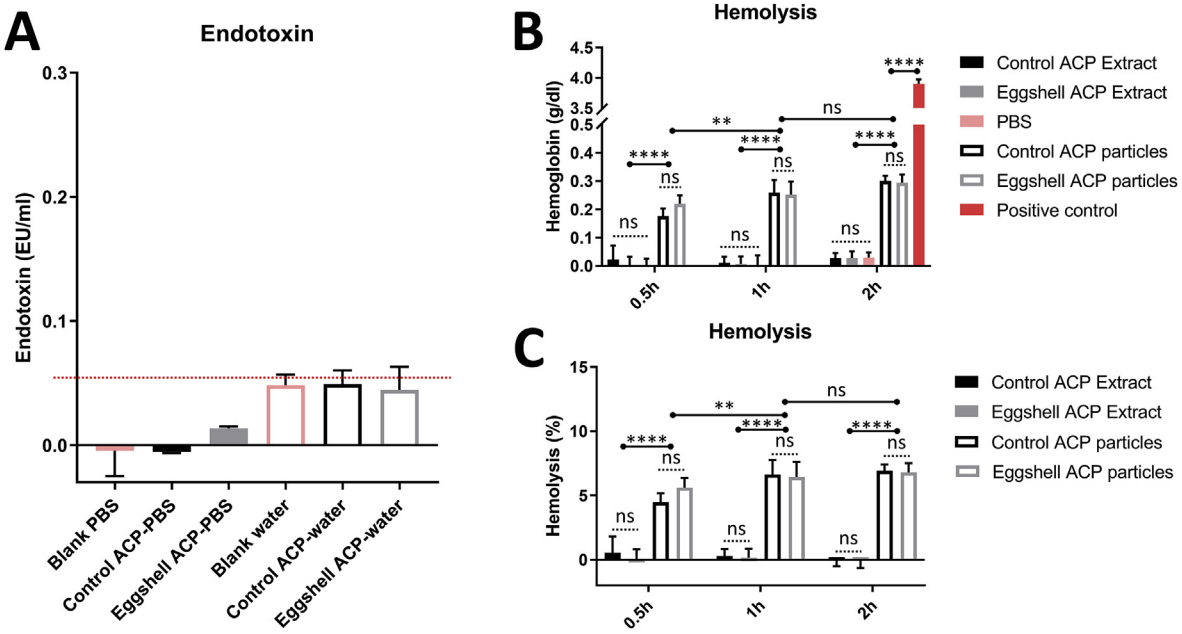

Fig. 4. Biosafety of ACP biomaterials. (A) Endotoxin contamination of ACP biomaterials, Red dot line, detection limitation threshold of LAL assay kit (0.05 EU/ml); (B) Hemoglobin release and (C) Hemolytic activity (%) of RBCs after contacting with ACP materials or ACP extracts. *, $p < 0.05$; **, $p < 0.01$; ***, $p < 0.001$; ****, $p < 0.0001$; ns, no significance.

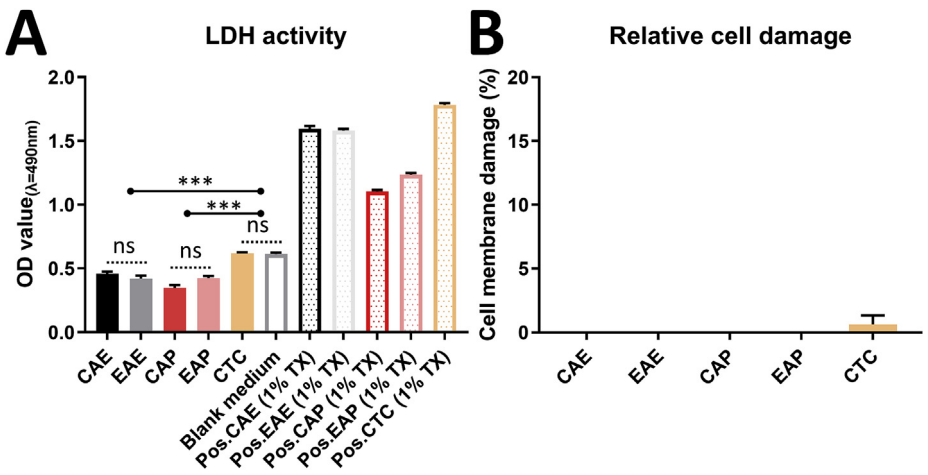

Fig. 5. Cytotoxicity of ACP biomaterials. (A) LDH release from THP-1 cells after cultured with ACP particles or ACP extracts for 48 h; (B) Relative cell damage (%) of THP-1 cells according to LDH activity. *, $p < 0.05$; **, $p < 0.01$; ***, $p < 0.001$; ****, $p < 0.0001$; ns, no significance.

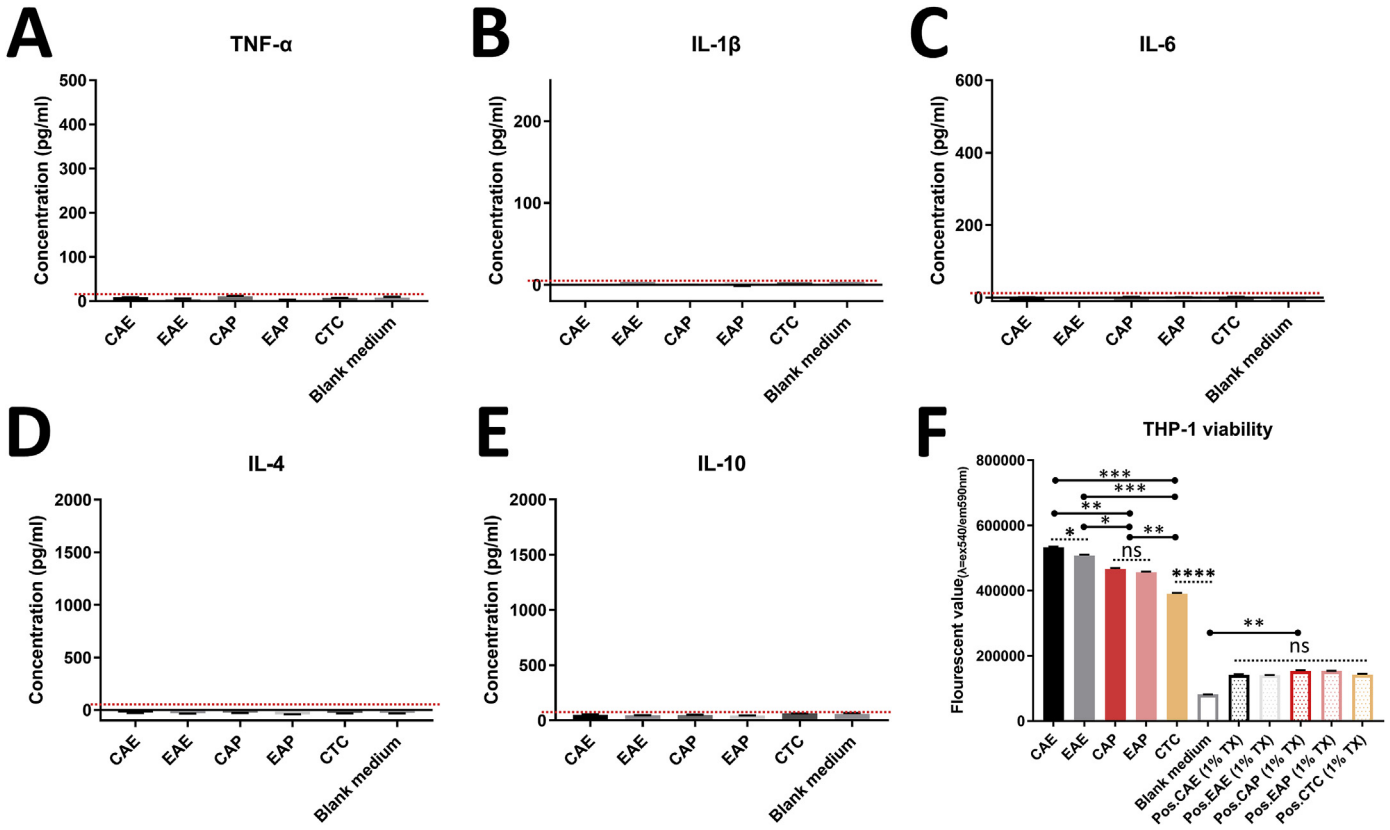

Fig. 6. Immunocompatibility and cytocompatibility of ACP biomaterials: (A–E) Inflammatory secretion and proliferation viability (F) from THP-1 cells after culturing with ACP powder/extracts for 48 h. (A) TNF-α; (B) IL-1β; (C) IL-6; (D) IL-4; (E) IL-10; (F) THP-1 cell proliferation viability by PrestoBlue assay. Red dot line, detection limitation threshold of ELISA kit (TNF-α: 15.625 ng/ml; IL-1β: 3.906 ng/ml; IL-6: 9.375 ng/ml; IL4: 31.250 ng/ml; IL-10: 31.250 ng/ml). *, $p < 0.05$; **, $p < 0.01$; ***, $p < 0.001$; ****, $p < 0.0001$; ns, no significance.

compared with the Control THP-1 cell group. The blank medium produced a weak fluorescent signal, and TritonX-100-induced LDH release did not affect the PrestoBlue reaction in the culture system (TritonX-100 groups in Figs. 5A and **6F**). Intriguingly, direct contact with ACP particles was likely to suppress THP-1 proliferation compared with ACP extracts, which may attribute to the limited space and nutrient supply around THP-1 cells.

3.3. Osteogenic activity of ACP Particles

3.3.1. Real-time quantitative PCR of osteogenic genes expression

3D spheroids could provide a practical strategy enabling the aggregation of cells/ECM components that mimic the natural bone tissue. Considering the significantly enhanced osteogenic differentiation of mouse dental papilla cells in 3D spheroids culture system [81], our present study established a low-cost strategy to obtain 3D osteoblastic

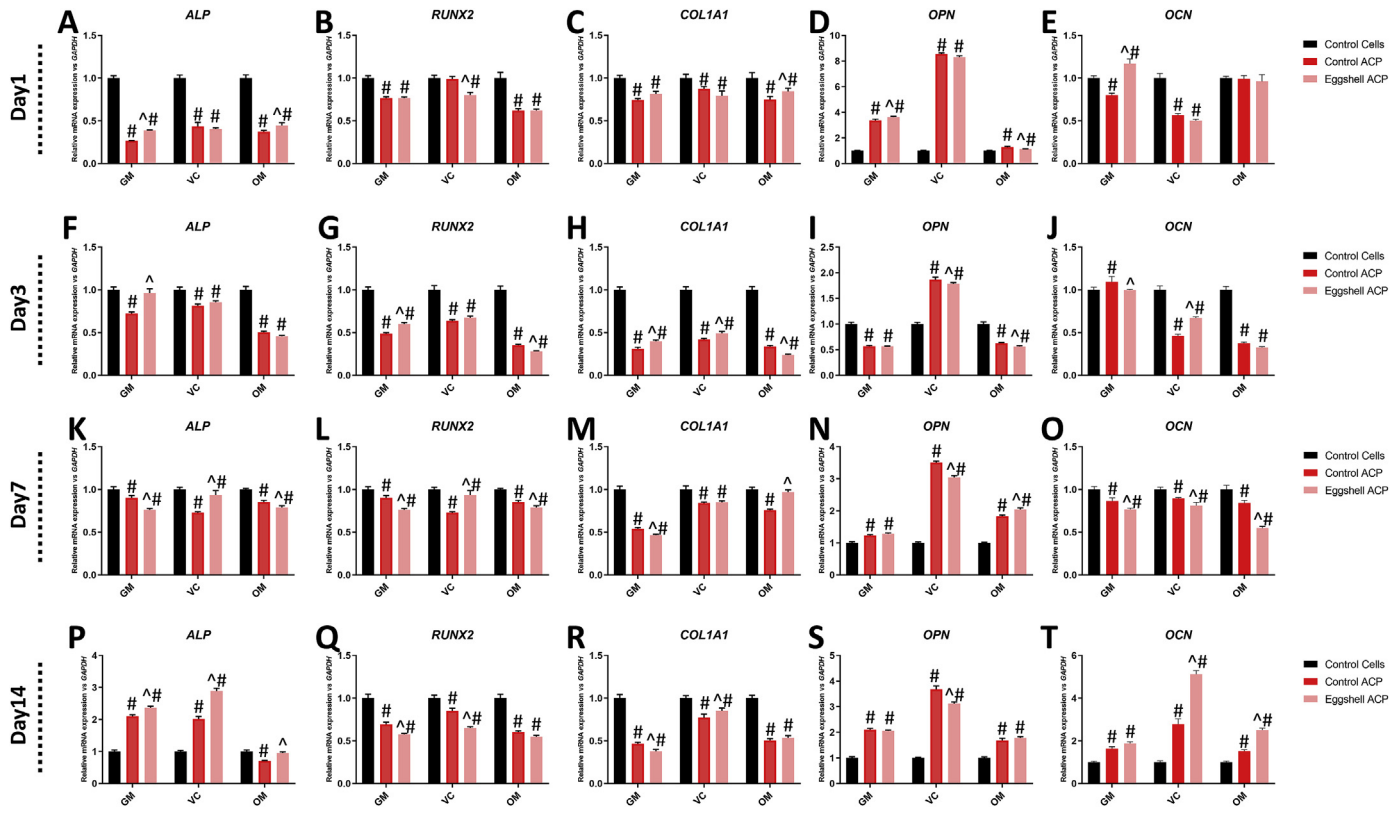

Fig. 7. Expression of osteogenic genes in MC-3T3-E1 cells in 3D spheroids embedded with ACP particles in different media. mRNA expression level of (A, F, K, P) *ALP*, (B, G, L, Q) *RUNX2*, (C, H, M, R) *COL1A1*, (D, I, N, S) *OPN,* and (E, J, O, T) *OCN* at indicated time points of day 1, 3, 7 and 14. $\#p < 0.01$ vs Control Cells; $\hat{}p < 0.01$ vs Control ACP.

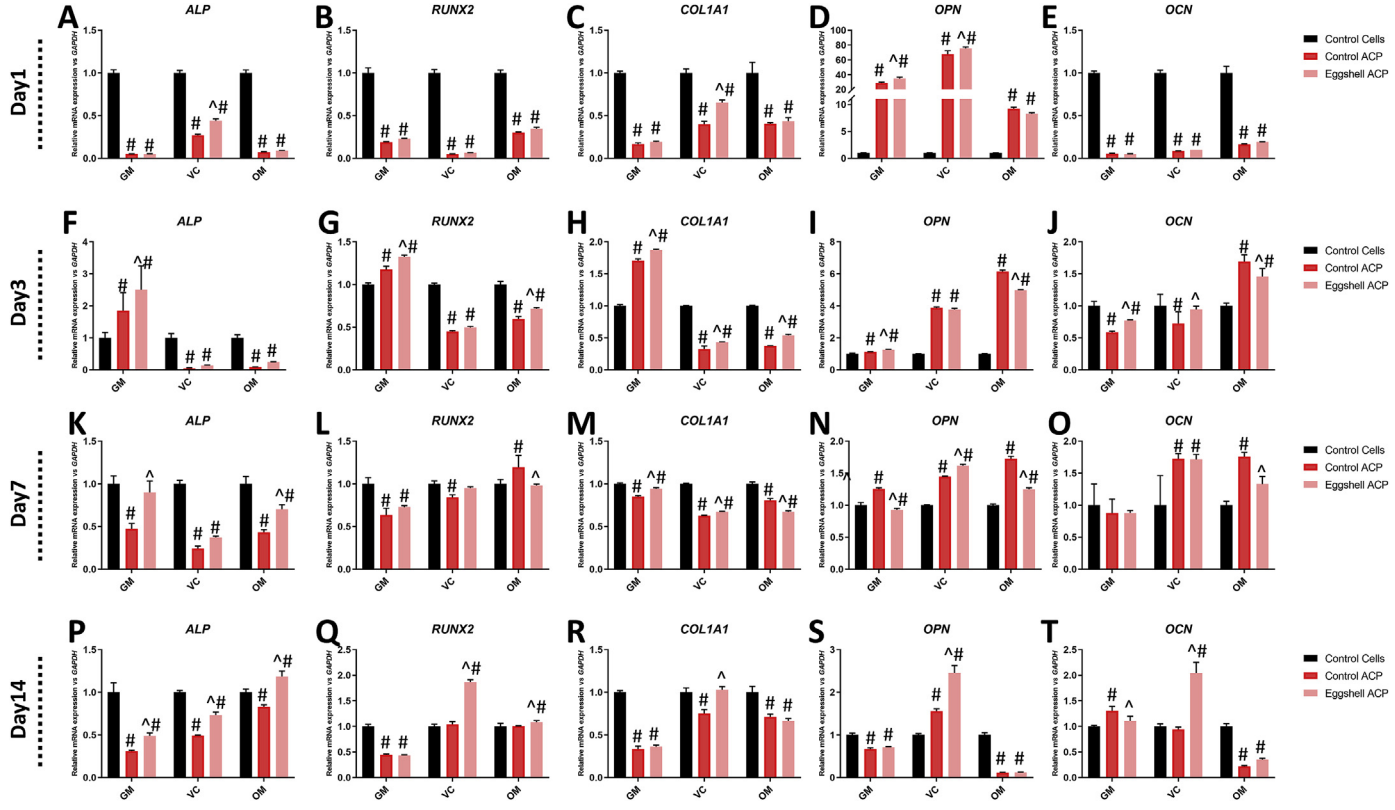

Fig. 8. Expression of osteogenic genes in MC-3T3-E1 cells cultured in a 2D system with ACP particles in different media. mRNA expression level of (A, F, K, P) *ALP*, (B, G, L, Q) *RUNX2*, (C, H, M, R) *COL1A1*, (D, I, N, S) *OPN,* and (E, J, O, T) *OCN* at indicated time points of day 1, 3, 7 and 14. $\#p < 0.01$ vs Control Cells; $\hat{}p < 0.01$ vs Control ACP.

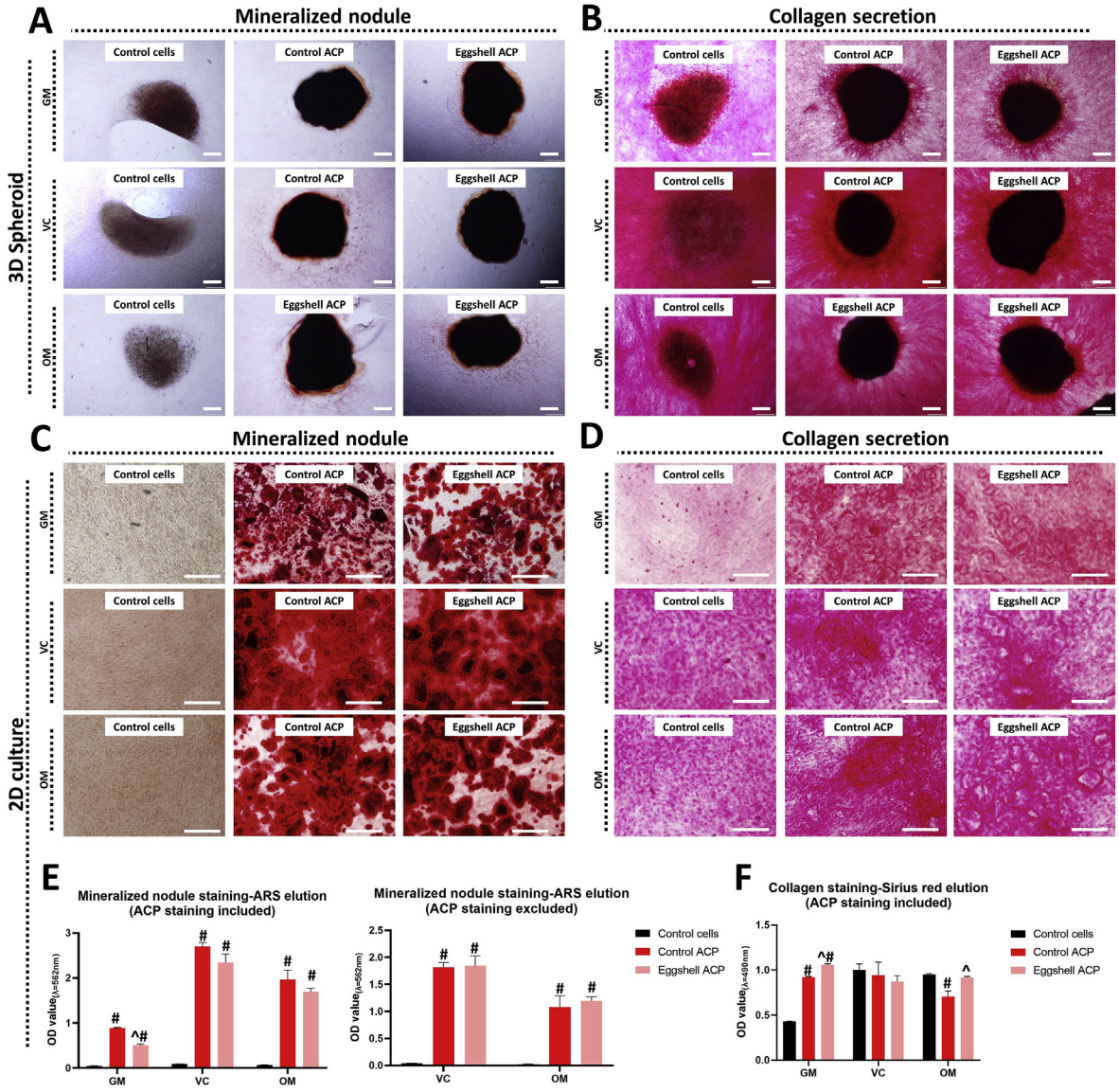

Fig. 9. ECM mineralization and collagens secretion of MC-3T3-E1 cells cultured in 3D spheroids with ACP particles embedded and 2D culture system for 14 days. (A) Alizarin Red S (ARS) staining for mineralized modules in 3D spheroids; (B) Sirius red staining for collagens secretion in 3D spheroids; (C) ARS staining for mineralized modules in 2D system; (D) Sirius red staining for collagens secretion in 2D culture system; (E) Total OD value and net OD value (after the subtraction of corresponding OD values in GM condition) of ARS staining in the eluents from the 2D system; (F) OD value of Sirius red in the eluents from the 2D system. Scale bar = 100 μm $\#p <$ 0.01 vs. Control Cells; $\hat{}p < 0.01$ vs. Control ACP.

spheroids based on non-adherent U bottom well plates with ACP particles embedded (**Flowchart**). The osteogenic inductive effects of ACP biomaterials on MC-3T3-E1 cells in osteoblastic spheroids and 2D culture systems were evaluated by qPCR. As plotted in Fig. 7 (Spheroids), osteogenic differentiation was studied under three conditions: GM, VC medium, and OM. In brief, both Control and Eggshell ACP particles effectively enhanced osteogenic gene expression in spheroids. Especially *OPN* (elevated from Day 7–21 during the mineralization of MT-3T3-E1 cells [82]), which was induced as high as 9 folds compared with the cell spheroids control (Fig. 7D, I, N, S). As an osteogenic maker of late-stage ECM mineralization, the mRNA level of *OCN* (elevated after Day 14 [82]) was also promoted by ACP particles in all media groups on Day 14 (Figure.7T). Although *ALP* (elevated on Day 3–14 [82]) expression was a little bit suppressed on Day 3 and 7, such suppressive effects of ACP particles greatly reduced with time and reversed to an up-regulative function at Day14 (Fig. 7A, F, K, P). On the contrary, *RUNX2* and *COL1A1* expressions were moderately inhibited at all time points. Notably, a high level of *RUNX2* is crucial for the differentiation from mesenchymal stem cells to immature osteoblasts [83]. For further bone maturation (immature osteoblasts to mature osteoblasts/osteocytes), *RUNX2* expression has to be downregulated [83]. Therefore, ACP particle embedding could contribute to the maturity of MC-3T3-E1 cells. Albeit a lower level of *COL1A1* might lead to reduced ECM deposition, the level, and arrangement of collagen fibrils in protein level was also essential for ECM mineralization and was investigated later.

Compared with the 3D spheroid model, the expression of osteogenic markers in the 2D culture system was different (Fig. 8). Both Control and Eggshell ACP particles could also promote the OPN expression at an early stage (Fig. 8D, I). However, such enhancement was weakened and even reversed to an inhibitive effect after Day 7 (Figure.8N, S). On the other hand, the suppressive effects of ACP particles on *OCN* expression on Day 1 were much stronger than that in the spheroids system (Figs. 7E and 8E). Similar improvement of *OCN* expression at Day 14 could be observed in both spheroids and 2D system (Figure.7T and 8T). The spheroids model and Eggshell ACP were more effective in inducing *OCN* expression than Control ACP and 2D culture. In the 2D culture system, more potent

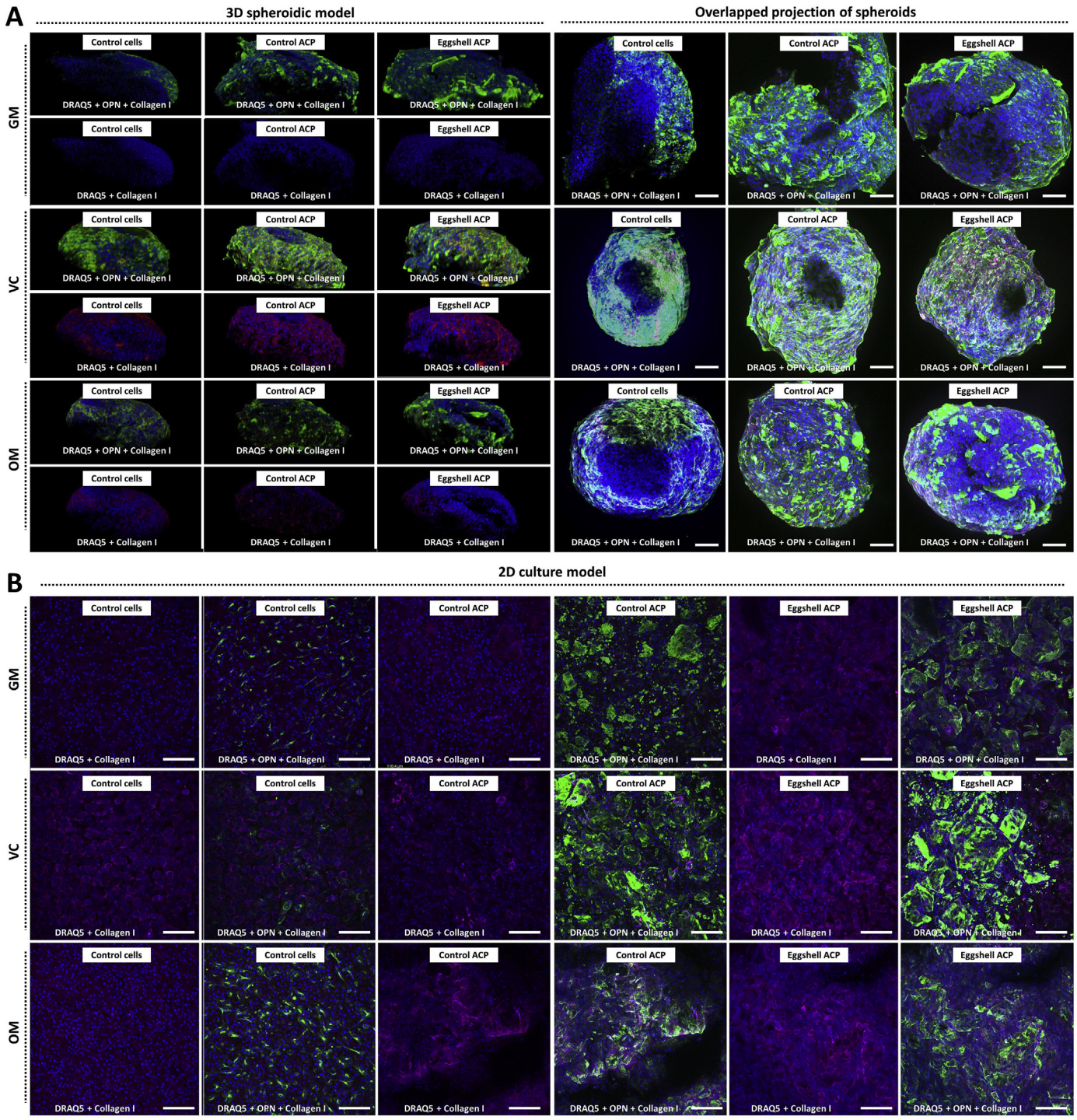

Fig. 10. Confocal microscopic inspection of OPN and collagen I expression of MC-3T3-E1 cells in 3D spheroids with ACP particles embedded and 2D culture system, respectively. (A) Left panel: OPN and collagen I expression in different culture media in 3D reconstructed images; Right panel: maximal fluorescent projection of OPN and collagen I in 3D spheroids as shown in left penal; (B) OPN and collagen I expression in different culture media in a 2D culture system. Scale bar = 100 μm.

inhibition could be found in *ALP* and *COL1A1* expression in ACP-treated groups than in the spheroids model (Fig. 8A-C). However, their inhibitive function on *RUNX2* was weaker than in the spheroids system (Fig. 8G and Q). The different mRNA expression patterns between spheroids and the 2D model (especially in the early stage) might attribute to the high dissolving capability of ACP materials. Once ACP particles come into contact with an aqueous environment, they rapidly start to dissolve, thus dramatically increasing Ca^{2+} and PO_4^{3+} concentrations in the medium. When encapsulated into the spheroids, When encapsulated inside the spheroids, layers of cells could hinder the release of ions from ACP particles. Conversely, Ca^{2+} and PO_4^{3+} ions could disperse in 2D culture freely, affecting cells not in contact with ACP particles. Such a hypothesis helps to explain different mRNA expression patterns in spheroids and 2D cultures [84,85]. In summary, the 3D spheroids system is more friendly for the osteogenic differentiation of MC-3T3-E1 cells. Both Control and Eggshell ACP particles could improve the osteogenic differentiation of osteoblasts. Eggshell ACP exhibited higher osteogenic activity, which may be due to its size, SSA, and elemental composition.

3.3.2. ECM mineralization staining and confocal microscope analysis

In addition to the expression of the osteogenic genes, the staining of ECM mineralization and extracellular collagens was further conducted to analyze the macroscopic osteogenic functions in spheroids and 2D culture. The as-build (instantly taken out from U-bottom plates) Control (693.24 ± 76.41 nm) and Eggshell ACP spheroids (715.19 ± 89.93 nm) were more prominent than the Control cells spheroids (483.67 ± 58.17 nm) but with a similar sphere shape. However, the spheroids altered their shape by cultivation on a planar surface. As it is shown in Fig. 9A, Control cells spheroids had difficulty keeping a round shape in all three media conditions. The cells on top of the spheroids were prone to "flow-down" and formed an "oblate" shape with loose intercellular connections. Both Control and Eggshell ACP embedded spheroids kept an original semi-spheric shape with condensed cell-materials connection in all media groups. Red ARS staining could be observed in all ACP-embedded spheroids rather than Control cells. Smaller mineralized nodules could also be found around these ACP spheroids in the OM group. The primary shortcoming of the spheroids ARS staining is the difficulty of distinguishing ACP particles inside. Therefore, we also set a parallel experiment to inspect the ARS staining around ACP particles in a 2D culture model. Abundant ARS staining was found in all ACP groups, while only a few small red dots were in the Control cells group in OM. The eluent analysis was conducted to measure semi-quantitatively the ARS staining of mineralized nodules. The results indicated that ACP particles improved the mineralized nodule formation effectively (Fig. 9E). Regarding that ARS staining may interfere with ACP particles rich in Ca^{2+}, the absorbance in the GM group (as baseline) was subtracted from VC and OM. Dramatically, the VC medium worked as the most efficient medium to induce ECM mineralization (VC > OM > GM). Similarly, VC medium led to the most collagens secretion compared with OM and GM (VC > OM > GM). In addition, ACP particles (both Control and Eggshell) could boost collagen production in all media groups (except Control ACP in OM, Fig. 9F). It is worth noting that collagen fibrils/bundles were formed around ACP particles. Such structure was similar to the primary network of CaP core/collagen fibrils in natural bone tissue. Nevertheless, such findings were not in accordance with the suppressive functions of ACP particles on *COL1A1* expression in qPCR assay (Figs. 7 and **8**). One possible explanation could be that the over-expressed OPN protein promoted the translation of collagen I by suppressing miR-129-5p expression. miR-129-5p directly targets the 3-UTR of *COL1A1* mRNA and exerts inhibitive functions on the post-transcriptional activities of *COL1A1*, thereby reducing the production of collagen I [86]. Moreover, OPN is also essential for the quality of collagen I fibril formation in bone tissue [87]. The formation of collagen bundles wrapped around ACP particles may be regulated by the level and distribution of OPN.

Immunofluorescent staining was performed on osteoblastic spheroids and 2D culture to clarify the expression and distribution pattern of OPN and type I collagen. Fig. 10A provided the 3D reconstruction of spheroids with OPN (green) and collagen I (red) staining. In the GM condition, the OPN expression was enhanced in Control and Eggshell ACP spheroids. OPN was found to be mostly located on the surface of ACP particles. Meanwhile, there was only weak collagen I staining in ACP spheroids rather than in Control cells. VC medium greatly enhanced the baseline level of OPN expression in all three groups. However, ACP particles still induced more OPN expression on their surface. Interestingly, more intense collagen I staining could be observed in Control and Eggshell ACP spheroids, partially overlapping with OPN staining (Fig. 10A, Overlapped projection). Eggshell ACP induced the most collagen I expression compared with other groups. Notably, OM did not further improve the OPN and collagen I expression compared with the VC medium. Since the spheroids were too thick to inspect the detailed OPN and collagen I distribution, a 2D culture model was employed to analyze their colocalization. As depicted in Fig. 10B, the VC medium similarly increased the collagen I expression more than other media. No colocalization of OPN and collagen I was found in the Control cells group. Control and Eggshell ACP induced intense OPN and collagen I deposition on the particle surfaces. However, it was worth noting that there was no overlap between OPN and collagen I of Control ACP in the VC medium.

4. Summary and conclusions

This study developed a dissolution-precipitation method to convert eggshells into endotoxin-free and immunocompatible ACP particles. Compared to the Control ACP, Eggshell ACP particles were more resistant to re-crystallization and exhibited ideal cytocompatibility. To better simulate the *in vivo* environment after the implantation of graft materials, an ACP-embedded 3D spheroidic model was established. Remarkably, Eggshell ACP particles induced typical mRNA expression profiles of osteogenic differentiation in 3D osteoblast spheroids, accompanied by the increased formation of mineralized nodules and up-regulated synthesis of ECM proteins represented by OPN and collagen I. In conclusion, our study provides a promising technique to synthesize high-value-added, osteoinductive ACP graft particles from eggshell waste. Furthermore, the osteoblastic spheroids constructed in this study provide a more practical model for biomaterial research, which can reflect the three-dimensional interaction between host bone tissue and graft materials more realistically.

Data availability

The raw data required to reproduce these findings cannot be shared at this time as the data also forms part of an ongoing study.

CRediT authorship contribution statement

Qianli Ma: Investigation, Methodology, Formal analysis, Validation, Data curation, Writing – original draft, Writing – review & editing. **Kristaps Rubenis:** Investigation, Formal analysis, Writing – original draft, Methodology. **Ólafur Eysteinn Sigurjónsson:** Funding acquisition, Methodology, Supervision. **Torben Hildebrand:** Investigation. **Therese Standal:** Resources, Writing – review & editing. **Signe Zemjane:** Investigation, Software. **Janis Locs:** Funding acquisition, Resources. **Dagnija Loca:** Funding acquisition, Conceptualization, Project administration, Visualization, Writing – review & editing. **Håvard Jostein Haugen:** Funding acquisition, Data curation, Visualization, Writing – review & editing.

Declaration of competing interest

The authors declare that they have no known competing financial interests or personal relationships that could have appeared to influence the work reported in this paper.

Acknowledgments

We acknowledge financial support from the Baltic Research Programme Project No. EEA-RESEARCH-85 "Waste-to-resource: eggshells as a source for next generation biomaterials for bone regeneration (EGGSHELL)" under the EEA Grant of Iceland, Liechtenstein and Norway No. EEZ/BPP/VIAA/2021/1 and National Natural Science Foundation of China (No. 81971752). The authors acknowledge the access to the infrastructure and expertise of the BBCE – Baltic Biomaterials Centre of Excellence (European Union's Horizon 2020 research and innovation programme under grant agreement No. 857287).

Appendix A. Supplementary data

Supplementary data to this article can be found online at https://doi.org/10.1016/j.smaim.2023.04.001.

References

[1] A.A. Jahangir, R.M. Nunley, S. Mehta, A. Sharan, Bone-graft substitutes in orthopaedic surgery, AAos now 2 (2008) 35–37.
[2] C. Laurencin, Y. Khan, S.F. El-Amin, Bone graft substitutes, Expet Rev. Med. Dev. 3 (2006) 49–57.
[3] J.T.B. Ratnayake, M. Mucalo, G.J. Dias, Substituted hydroxyapatites for bone regeneration: a review of current trends, J. Biomed. Mater. Res. B Appl. Biomater. 105 (2017) 1285–1299.
[4] Y. Yang, W. Luan, Y. Xue, Sustainability and environmental inequality: effects of animal husbandry pollution in China, Sustainability 11 (2019) 4576.
[5] G. Koneswaran, D. Nierenberg, Global farm animal production and global warming: impacting and mitigating climate change, Environ. Health Perspect. 116 (2008) 578–582.
[6] E. Tullo, A. Finzi, M. Guarino, Environmental impact of livestock farming and Precision Livestock Farming as a mitigation strategy, Sci. Total Environ. 650 (2019) 2751–2760.
[7] R. Florencio-Silva, G.R.D. Sasso, E. Sasso-Cerri, M.J. Simoes, P.S. Cerri, Biology of bone tissue: structure, function, and factors that influence bone cells, BioMed Res. Int. (2015), 2015.
[8] S.V. Dorozhkin, Biphasic, triphasic and multiphasic calcium orthophosphates, Acta Biomater. 8 (2012) 963–977.
[9] E.R. Luvizuto, S. Tangl, G. Zanoni, T. Okamoto, C.K. Sonoda, R. Gruber, R. Okamoto, The effect of BMP-2 on the osteoconductive properties of beta-tricalcium phosphate in rat calvaria defects, Biomaterials 32 (2011) 3855–3861.
[10] H. Choi, N.J. Park, O. Jamiyandorj, M.H. Hong, S. Oh, Y.B. Park, S. Kim, Improvement of osteogenic potential of biphasic calcium phosphate bone substitute coated with synthetic cell binding peptide sequences, J. Periodontal. Implant Sci. 42 (2012) 166–172.
[11] S.V. Dorozhkin, M. Epple, Biological and medical significance of calcium phosphates, Angew. Chem. Int. Ed. 41 (2002) 3130–3146.
[12] C.J. Oosterbos, A.I. Rahmy, A.J. Tonino, W. Witpeerd, High survival rate of hydroxyapatite-coated hip prostheses: 100 consecutive hips followed for 10 years, Acta Orthop. Scand. 75 (2004) 127–133.
[13] W. He, M. Andersson, P.P. de Souza, C.A. de Souza Costa, E.M. Munoz, H.O. Schwartz-Filho, M. Hayashi, A. Hemdal, A. Fredel, A. Wennerberg, R. Jimbo, Osteogenesis-inducing calcium phosphate nanoparticle precursors applied to titanium surfaces, Biomed. Mater. 8 (2013), 035007.
[14] B. Sarikaya, H.M. Aydin, Collagen/beta-tricalcium phosphate based synthetic bone grafts via dehydrothermal processing, BioMed Res. Int. (2015), 2015.
[15] D. Bellucci, A. Sola, V. Cannillo, Hydroxyapatite and tricalcium phosphate composites with bioactive glass as second phase: state of the art and current applications, J. Biomed. Mater. Res. 104 (2016) 1030–1056.
[16] B. Enkel, C. Dupas, V. Armengol, J. Akpe Adou, J. Bosco, G. Daculsi, A. Jean, O. Laboux, R.Z. LeGeros, P. Weiss, Bioactive materials in endodontics, Expet Rev. Med. Dev. 5 (2008) 475–494.
[17] T. Feenstra, P. De Bruyn, Formation of calcium phosphates in moderately supersaturated solutions, J. Phys. Chem. 83 (1979) 475–479.
[18] S.V. Dorozhkin, Amorphous calcium (ortho)phosphates, Acta Biomater. 6 (2010) 4457–4475.
[19] L. Chen, P. Qiao, H. Liu, L. Shao, Amorphous calcium phosphate NPs mediate the macrophage response and modulate BMSC osteogenesis, Inflammation 44 (2021) 278–296.
[20] R.Z. LeGeros, Properties of Osteoconductive Biomaterials: Calcium Phosphates, Clinical Orthopaedics and Related Research, 2002, pp. 81–98.
[21] J. Mahamid, A. Sharir, L. Addadi, S. Weiner, Amorphous calcium phosphate is a major component of the forming fin bones of zebrafish: indications for an amorphous precursor phase, Proc. Natl. Acad. Sci. USA 105 (2008) 12748–12753.
[22] F. Nudelman, K. Pieterse, A. George, P.H. Bomans, H. Friedrich, L.J. Brylka, P.A. Hilbers, G. de With, N.A. Sommerdijk, The role of collagen in bone apatite formation in the presence of hydroxyapatite nucleation inhibitors, Nat. Mater. 9 (2010) 1004–1009.
[23] J. Mahamid, B. Aichmayer, E. Shimoni, R. Ziblat, C. Li, S. Siegel, O. Paris, P. Fratzl, S. Weiner, L. Addadi, Mapping amorphous calcium phosphate transformation into crystalline mineral from the cell to the bone in zebrafish fin rays, Proc. Natl. Acad. Sci. USA 107 (2010) 6316–6321.
[24] J. Mahamid, A. Sharir, D. Gur, E. Zelzer, L. Addadi, S. Weiner, Bone mineralization proceeds through intracellular calcium phosphate loaded vesicles: a cryo-electron microscopy study, J. Struct. Biol. 174 (2011) 527–535.
[25] S. Boonrungsiman, E. Gentleman, R. Carzaniga, N.D. Evans, D.W. McComb, A.E. Porter, M.M. Stevens, The role of intracellular calcium phosphate in osteoblast-mediated bone apatite formation, Proc. Natl. Acad. Sci. USA 109 (2012) 14170–14175.
[26] M. Kerschnitzki, A. Akiva, A.B. Shoham, Y. Asscher, W. Wagermaier, P. Fratzl, L. Addadi, S. Weiner, Bone mineralization pathways during the rapid growth of embryonic chicken long bones, J. Struct. Biol. 195 (2016) 82–92.
[27] K. Nitiputri, Q.M. Ramasse, H. Autefage, C.M. McGilvery, S. Boonrungsiman, N.D. Evans, M.M. Stevens, A.E. Porter, Nanoanalytical electron microscopy reveals a sequential mineralization process involving carbonate-containing amorphous precursors, ACS Nano 10 (2016) 6826–6835.
[28] X. Cai, B. Han, Y. Liu, F. Tian, F. Liang, X. Wang, Chlorhexidine-Loaded amorphous calcium phosphate nanoparticles for inhibiting degradation and inducing mineralization of type I collagen, ACS Appl. Mater. Interfaces 9 (2017) 12949–12958.
[29] J.R. Popp, K.E. Laflin, B.J. Love, A.S. Goldstein, In vitro evaluation of osteoblastic differentiation on amorphous calcium phosphate-decorated poly (lactic-co-glycolic acid) scaffolds, J. Tissue Eng. Regenerative Med. 5 (2011) 780–789.
[30] S. Allegrini, A.C. da Silva, M. Tsujita, M.B. Salles, S.A. Gehrke, F.J.C. Braga, Amorphous calcium phosphate (ACP) in tissue repair process, Microsc. Res. Tech. 81 (2018) 579–589.
[31] B.M. Whited, D. Skrtic, B.J. Love, A.S. Goldstein, Osteoblast response to zirconia-hybridized pyrophosphate-stabilized amorphous calcium phosphate, J. Biomed. Mater. Res. 76 (2006) 596–604.
[32] T.H. Qaid, S. Ramesh, F. Yusof, W.J. Basirun, Y.C. Ching, H. Chandran, S. Ramesh, S. Krishnasamy, Micro-arc oxidation of bioceramic coatings containing eggshell-derived hydroxyapatite on titanium substrate, Ceram. Int. 45 (2019) 18371–18381.
[33] W. Wang, L. Zhao, K. Wu, Q. Ma, S. Mei, P.K. Chu, Q. Wang, Y. Zhang, The role of integrin-linked kinase/beta-catenin pathway in the enhanced MG63 differentiation by micro/nano-textured topography, Biomaterials 34 (2013) 631–640.
[34] I. Zofkova, P. Nemcikova, P. Matucha, Trace elements and bone health, Clin. Chem. Lab. Med. 51 (2013) 1555–1561.
[35] S. Mahdavi, A. Amirsadeghi, A. Jafari, S.V. Niknezhad, S.A. Bencherif, Avian egg: a multifaceted biomaterial for tissue engineering, Ind. Eng. Chem. Res. 60 (2021) 17348–17364.
[36] S.J. Lee, S.H. Oh, Fabrication of calcium phosphate bioceramics by using eggshell and phosphoric acid, Mater. Lett. 57 (2003) 4570–4574.
[37] G. Gergely, F. Wéber, I. Lukács, A.L. Tóth, Z.E. Horváth, J. Mihály, C. Balázsi, Preparation and characterization of hydroxyapatite from eggshell, Ceram. Int. 36 (2010) 803–806.
[38] M.M. Rahman, A.N. Netravali, B.J. Tiimob, V. Apalangya, V.K. Rangari, Bio-inspired " green" nanocomposite using hydroxyapatite synthesized from eggshell waste and soy protein, J. Appl. Polym. Sci. 133 (2016).
[39] P.S. Guru, S. Dash, Sorption on eggshell waste—a review on ultrastructure, biomineralization and other applications, Adv. Colloid Interface Sci. 209 (2014) 49–67.
[40] D.K. Patel, B. Jin, S.D. Dutta, K.-T. Lim, Osteogenic potential of human mesenchymal stem cells on eggshells-derived hydroxyapatite nanoparticles for tissue engineering, J. Biomed. Mater. Res. B Appl. Biomater. 108 (2020) 1953–1960.
[41] C.B. Zanelato, A.F. Pires, S.N. da Silva, A.G.S. Galdino, Development of biphasic bone cement obtained from chicken eggshell, J. Mater. Res. Technol. 9 (2020) 7297–7304.
[42] T.S. Sampath Kumar, K. Madhumathi, B. Rajkamal, S. Zaheatha, A. Rajathi Malar, S. Alamelu Bai, Enhanced protein delivery by multi-ion containing eggshell derived apatitic-alginate composite nanocarriers, Colloids Surf. B Biointerfaces 123 (2014) 542–548.
[43] R. Jayasree, S. Indrakumar, D. Rana, M. Ramalingam, T. Kumar, Bone mineral-like nanoscale amorphous calcium phosphate derived from egg shells, J. Bionanoscience 11 (2017) 297–300.
[44] C. Combes, C. Rey, Amorphous calcium phosphates: synthesis, properties and uses in biomaterials, Acta Biomater. 6 (2010) 3362–3378.
[45] A.L. Boskey, A.S. Posner, Magnesium stabilization of amorphous calcium-phosphate - kinetic study, Mater. Res. Bull. 9 (1974) 907–916.
[46] H.C. Ding, H.H. Pan, X.R. Xu, R.K. Tang, Toward a detailed understanding of magnesium ions on hydroxyapatite crystallization inhibition, Cryst. Growth Des. 14 (2014) 763–769.
[47] M.W. Laschke, M.D. Menger, Life is 3D: boosting spheroid function for tissue engineering, Trends Biotechnol. 35 (2017) 133–144.
[48] F. Pampaloni, E.G. Reynaud, E.H.K. Stelzer, The third dimension bridges the gap between cell culture and live tissue, Nat. Rev. Mol. Cell Biol. 8 (2007) 839–845.
[49] L.G. Griffith, M.A. Swartz, Capturing complex 3D tissue physiology in vitro, Nat. Rev. Mol. Cell Biol. 7 (2006) 211–224.
[50] E. Fennema, N. Rivron, J. Rouwkema, C. van Blitterswijk, J. de Boer, Spheroid culture as a tool for creating 3D complex tissues, Trends Biotechnol. 31 (2013) 108–115.
[51] M. Nowacka, K. Sterzynska, M. Andrzejewska, M. Nowicki, R. Januchowski, Drug resistance evaluation in novel 3D in vitro model, Biomed. Pharmacother. 138 (2021).
[52] L.F. Yu, M.C.W. Chen, K.C. Cheung, Droplet-based microfluidic system for multicellular tumor spheroid formation and anticancer drug testing, Lab Chip 10 (2010) 2424–2432.
[53] R.Z. Lin, H.Y. Chang, Recent advances in three-dimensional multicellular spheroid culture for biomedical research, Biotechnol. J. 3 (2008) 1172–1184.
[54] J.W. Haycock, 3D cell culture: a review of current approaches and techniques, Methods Mol. Biol. 695 (2011) 1–15.
[55] I. Gaitan-Salvatella, E.O. Lopez-Villegas, P. Gonzalez-Alva, F. Susate-Olmos, M.A. Alvarez-Perez, Case report: formation of 3D osteoblast spheroid under magnetic levitation for bone tissue engineering, Front. Mol. Biosci. 8 (2021).
[56] T. Anada, J. Fukuda, Y. Sai, O. Suzuki, An oxygen-permeable spheroid culture system for the prevention of central hypoxia and necrosis of spheroids, Biomaterials 33 (2012) 8430–8441.
[57] A. Asthana, W.S. Kisaalita, Microtissue size and hypoxia in HTS with 3D cultures, Drug Discov. Today 17 (2012) 810–817.
[58] J. Vecstaudza, J. Locs, Novel preparation route of stable amorphous calcium phosphate nanoparticles with high specific surface area, J. Alloys Compd. 700 (2017) 215–222.
[59] S. Brunauer, P.H. Emmett, E. Teller, Adsorption of gases in multimolecular layers, J. Am. Chem. Soc. 60 (1938) 309–319.
[60] International Organization for Standardization, ISO 10993-5, Biological Evaluation of Medical Devices. Part 5: Tests for in Vitro Cytotoxicity, 2009.

[61] E. Berger, D. Breznan, S. Stals, V.J. Jasinghe, D. Gonçalves, D. Girard, S. Faucher, R. Vincent, A.R. Thierry, C. Lavigne, Cytotoxicity assessment, inflammatory properties, and cellular uptake of Neutraplex lipid-based nanoparticles in THP-1 monocyte-derived macrophages, Nanobiomedicine (Rij) 4 (2017), 1849543517746259.
[62] C. Mochales, R.M. Wilson, S.E.P. Dowker, M.P. Ginebra, Dry mechanosynthesis of nanocrystalline calcium deficient hydroxyapatite: structural characterisation, J. Alloys Compd. 509 (2011) 7389–7394.
[63] C. Su, D.L. Suarez, In situ infrared speciation of adsorbed carbonate on aluminum and iron oxides, Clay Clay Miner. 45 (1997) 814–825.
[64] C. Ortali, I. Julien, C. Drouet, E. Champion, Influence of carbonation on the low-temperature consolidation by Spark Plasma Sintering of carbonated calcium phosphate bioceramics, Ceram. Int. 46 (2020) 5799–5810.
[65] C.C. Hung, A. Chaya, K. Liu, K. Verdelis, C. Sfeir, The role of magnesium ions in bone regeneration involves the canonical Wnt signaling pathway, Acta Biomater. 98 (2019) 246–255.
[66] N. Neves, D. Linhares, G. Costa, C.C. Ribeiro, M.A. Barbosa, In vivo and clinical application of strontium-enriched biomaterials for bone regeneration: a systematic review, Bone Joint. Res. 6 (2017) 366–375.
[67] T. Diamond, R. Pojer, D. Stiel, A. Alfrey, S. Posen, Does iron affect osteoblast function? Studies In vitro and in patients with chronic liver disease, Calcif. Tissue Int. 48 (1991) 373–379.
[68] J.G. Messer, A.K. Kilbarger, K.M. Erikson, D.E. Kipp, Iron overload alters iron-regulatory genes and proteins, down-regulates osteoblastic phenotype, and is associated with apoptosis in fetal rat calvaria cultures, Bone 45 (2009) 972–979.
[69] P. Jia, Y.J. Xu, Z.L. Zhang, K. Li, B.Y. Li, W. Zhang, H.L. Yang, Ferric ion could facilitate osteoclast differentiation and bone resorption through the production of reactive oxygen species, J. Orthop. Res. 30 (2012) 1843–1852.
[70] M.T. Fulmer, I.C. Ison, C.R. Hankermayer, B.R. Constantz, J. Ross, Measurements of the solubilities and dissolution rates of several hydroxyapatites, Biomaterials 23 (2002) 751–755.
[71] K. Rubenis, S. Zemjane, J. Vecstaudza, J. Bitenieks, J. Locs, Densification of amorphous calcium phosphate using principles of the cold sintering process, J. Eur. Ceram. Soc. 41 (2021) 912–919.
[72] M.J. Root, Inhibition of the amorphous calcium-phosphate phase-transformation reaction by polyphosphates and metal-ions, Calcif. Tissue Int. 47 (1990) 112–116.
[73] W. Jin, Z. Liu, Y. Wu, B. Jin, C. Shao, X. Xu, R. Tang, H. Pan, Synergic effect of Sr2+ and Mg2+ on the stabilization of amorphous calcium phosphate, Cryst. Growth Des. 18 (2018) 6054–6060.
[74] T.Y. Peng, P.Y. Tsai, M.S. Chen, Y. Mine, S.H. Wu, C.Y. Chen, D.J. Lin, C.K. Lin, Mesoporous properties of bioactive glass synthesized by spray pyrolysis with various polyethylene glycol and acid additions, Polymers 13 (2021).
[75] S. Allegrini Jr., A.C. da Silva, M. Tsujita, M.B. Salles, S.A. Gehrke, F.J.C. Braga, Amorphous calcium phosphate (ACP) in tissue repair process, Microsc. Res. Tech. 81 (2018) 579–589.
[76] F. Velard, J. Braux, J. Amedee, P. Laquerriere, Inflammatory cell response to calcium phosphate biomaterial particles: an overview, Acta Biomater. 9 (2013) 4956–4963.
[77] F. Velard, D. Laurent-Maquin, C. Guillaume, S. Bouthors, E. Jallot, J.M. Nedelec, A. Belaaouaj, P. Laquerriere, Polymorphonuclear neutrophil response to hydroxyapatite particles, implication in acute inflammatory reaction, Acta Biomater. 5 (2009) 1708–1715.
[78] P. Laquerriere, A. Grandjean-Laquerriere, S. Addadi-Rebbah, E. Jallot, D. Laurent-Maquin, P. Frayssinet, M. Guenounou, MMP-2, MMP-9 and their inhibitors TIMP-2 and TIMP-1 production by human monocytes in vitro in the presence of different forms of hydroxyapatite particles, Biomaterials 25 (2004) 2515–2524.
[79] G.K. Feng, C.S. Qin, X. Yi, J.G. Xia, J.J. Chen, X.Y. Chen, T. Chen, X.J. Jiang, Effect of novel bioresorbable scaffold composed of poly-l-lactic acid and amorphous calcium phosphate nanoparticles on inflammation and calcification of surrounding tissues after implantation, J. Mater. Sci. Mater. Med. 29 (2018).
[80] E. Buache, F. Velard, E. Bauden, C. Guillaume, E. Jallot, J.M. Nedelec, D. Laurent-Maquin, P. Laquerriere, Effect of strontium-substituted biphasic calcium phosphate on inflammatory mediators production by human monocytes, Acta Biomater. 8 (2012) 3113–3119.
[81] M. Yamamoto, N. Kawashima, N. Takashino, Y. Koizumi, K. Takimoto, N. Suzuki, M. Saito, H. Suda, Three-dimensional spheroid culture promotes odonto/osteoblastic differentiation of dental pulp cells, Arch. Oral Biol. 59 (2014) 310–317.
[82] G.R. Beck, B. Zerler, E. Moran, Phosphate is a specific signal for induction of osteopontin gene expression, Proc. Natl. Acad. Sci. U. S. A 97 (2000) 8352–8357.
[83] M. Bruderer, R.G. Richards, M. Alini, M.J. Stoddart, Role and regulation of Runx2 in osteogenesis, Eur. Cell. Mater. 28 (2014) 269–286.
[84] M.N. Lee, H.S. Hwang, S.H. Oh, A. Roshanzadeh, J.W. Kim, J.H. Song, E.S. Kim, J.T. Koh, Elevated extracellular calcium ions promote proliferation and migration of mesenchymal stem cells via increasing osteopontin expression, Exp. Mol. Med. 50 (2018).
[85] S.F. An, Y. Gao, J.Q. Ling, Characterization of human periodontal ligament cells cultured on three-dimensional biphasic calcium phosphate scaffolds in the presence and absence of L-ascorbic acid, dexamethasone and beta-glycerophosphate in vitro, Exp. Ther. Med. 10 (2015) 1387–1393.
[86] Y.H. Chen, Y.T. Ou, J.L. Dong, G.Z. Yang, Z. Zeng, Y. Liu, B. Liu, W.D. Li, X.S. He, T. Lan, Osteopontin promotes collagen I synthesis in hepatic stellate cells by miRNA-129-5p inhibition (vol 362, pg 343, 2018), Exp. Cell Res. 363 (2018), 140-140.
[87] B. Depalle, C.M. McGilvery, S. Nobakhti, N. Aldegaither, S.J. Shefelbine, A.E. Porter, Osteopontin regulates type I collagen fibril formation in bone tissue, Acta Biomater. 120 (2021) 194–202.